In press at G-Cubed, September 2026, doi:10.1029/2026GC013003.
manuscript submitted to *Geochemistry, Geophysics, Geosystems*

Full-waveform Seismic Tomography of the Upper Mantle Beneath the Arabia-Eurasia Collision Zone

Edward J. Clennett[1,2], Chujie Liu[1,3], Stephen P. Grand[1], and Thorsten W. Becker[1,2,4]

[1]Department of Earth and Planetary Sciences, Jackson School of Geosciences, The University of Texas at Austin, Austin, TX, USA
[2]Institute for Geophysics, Jackson School of Geosciences, The University of Texas at Austin, Austin, TX, USA
[3]Department of Earth Sciences, University of Buffalo, Buffalo, NY, USA
[4]Oden Institute for Computational Engineering and Sciences, The University of Texas at Austin, Austin, TX, USA

Key Points:

- We present a new full-waveform seismic velocity model for the Middle East region, called FWME24.
- We image processes including craton underthrusting, continental subduction and lithospheric delamination.
- Reconstructing the underthrusting of Arabia back in time indicates that the Arabia-Eurasia collision initiated at ∼22 Ma.

Corresponding author: Edward Clennett, edward.clennett@utexas.edu

Abstract

Despite being one of the most recent major orogenic events, the timing of the Arabia-Eurasia collision is still debated. Much of the discrepancy arises due to uncertainties over the amount of continental subduction of the Arabian passive margin and the timing of a hard collision of cratonic Arabian lithosphere with Eurasia. Subducted continental lithosphere and underthrusted cratons can be imaged using high resolution seismic tomography, which can be used to improve understanding of the tectonic history of the region. In this study, we perform a full waveform inversion of seismic wave velocity beneath the Turkish-Iranian plateau, using regional earthquakes, which provide good horizontal and vertical resolution in the upper 500 km of the mantle. We use a normalized cross-correlation misfit function, which fits both the phase and relative amplitude of multi-path arrivals, allowing us to extract additional information from complex triplicated waves that provide relatively good coverage of the upper mantle. Our results reveal that 250 km thick Arabian lithosphere extends horizontally beneath Eurasia. When reconstructed back in time, these results indicate that continental underthrusting and collision initiated at ∼22 Ma, which is consistent with accelerated deformation observed at this time in the geological record.

Plain Language Summary

The ongoing collision between the Arabian and Eurasian tectonic plates has led to the formation of major mountain ranges including the Zagros, Alborz and Caucasus Mountains. Although we know that this collision started within the last 50 million years, the exact timing is debated – mostly due to uncertainty surrounding the original size of Arabia. Here, we used seismic waves to image Earth's upper mantle beneath the Middle East and estimate the original size of Arabia. By modelling waveforms and fitting their shapes to observations from seismometers, we develop a new seismic wavespeed model for the Middle East region with good resolution for the upper mantle. We use this to find part of the Arabian continent that is now beneath Eurasia. By reconstructing the motion of the Arabian plate, we estimated how long Arabia has been sliding beneath Eurasia. Undoing this motion indicates that Arabia would have started colliding with Eurasia around 22 million years ago.

1 Introduction

The collision between the Arabian and Eurasian plates has created one of Earth's major orogenic belts, comprising the Zagros, Alborz and Caucasus Mountains and the Turkish-Iranian plateau. Despite being one of the most recent orogenic events, the timing of collision remains enigmatic, with estimates ranging from the late Cretaceous to the Pliocene (e.g., Alavi, 1994; Guest et al., 2006). The ages are based on various lines of evidence, such as: the timing of thrusting, which has been dated to as old as 50 Ma (Alavi, 1994); the slowdown of the African plate at ∼35-30 Ma (Jolivet & Faccenna, 2000); restoration of shortening and continental subduction, which results in a 27 Ma collision date (McQuarrie & van Hinsbergen, 2013); increase in sedimentation rates at 20 Ma (e.g., Ballato et al., 2011); and the timing of uplift and exhumation determined with thermochronology, which gives ages as young as 12 Ma (Guest et al., 2006). Ballato et al. (2011) reconciled some of this variation by proposing a two-stage collision model, with earlier dates ∼35 Ma reflecting a soft collision of thinned continental lithosphere, and later dates from 20 Ma recording the arrival of thick continental lithosphere. However, estimating the timing of the initial soft collision is challenging as almost all of the thinned lithosphere has been subducted. Previous attempts to quantify the volume of thinned continental lithosphere have examined exposed Arabian passive margin in the eastern Mediterranean (Inati et al., 2016; Darin & Umhoefer, 2022) or the extent of ophiolite obduction in Oman (McQuarrie & van Hinsbergen, 2013), and extrapolated across the entire continent. In contrast, seis-

mic tomography images provide large-scale constraints on the volume and geometry of subducted lithosphere, which could help us to estimate the timing of the Arabia-Eurasia collision.

Seismic tomography has become an important tool in constraining tectonic history. Different methods include estimating slab sinking rates to determine the location and timing of past subduction zones (e.g., Ricard et al., 1993; van der Meer et al., 2010; Sigloch & Mihalynuk, 2013, 2017; Clennett et al., 2020), unfolding slabs to estimate the volume of subducted lithosphere (e.g., Wu et al., 2016; Chen et al., 2019; Fuston & Wu, 2020), or comparing seismic images with forward-modelled mantle structure (e.g., Bunge & Grand, 2000; Hafkenscheid et al., 2006; Steinberger et al., 2012). Such approaches have been applied to the Middle East region, considering both the earlier history of Neotethys subduction as well as detailed regional mantle structure beneath different parts of the Arabia-Eurasia Collision. Hafkenscheid et al. (2006) tested different tectonic scenarios for the closure of the Neotethys ocean, finding that the presence of a large, Early Cretaceous back-arc basin – called the Semail ocean after the large ophiolite in Oman – best explains the lower mantle structure. They also investigated the timing of the Arabia-Eurasia collision by estimating slab break off timings from slab sinking rates. In Anatolia, the western edge of the collision, Kounoudis et al. (2020) imaged the detached Bitlis slab in detail, arriving at a 28 Ma timing of break-off. Using receiver function analysis of the entire collision region, Kaviani et al. (2018) determined that the Tethyan slab is highly segmented, suggesting multiple ages of slab break-off and a diachronous Arabia-Eurasia collision. However, uncertainties in slab sinking rates could have a major effect on the estimated collision times using these methods (e.g., Steinberger et al., 2012).

Recent advances in full-waveform seismic tomography have allowed for higher-resolution imaging of upper mantle structure, in particular for settings where ray path coverage makes traditional ray path approaches challenging (e.g., Fichtner et al., 2009; Tao et al., 2017). By fitting triplicated waves that sample the upper mantle, Tao et al. (2017, 2018) extracted additional waveform information from regional earthquakes. The images show sharp and strong velocity anomalies of slabs such that the slab thickness is consistent with oceanic lithosphere and have seismic amplitude close to thermal model predictions of slabs. Extending this method to include the Himalayan region, Liu et al. (2024) produced a detailed image of the mantle structures beneath the India-Asia collision zone; this revealed the underthrusting of the Indian cratonic lithosphere beneath Tibet and subducted and detached non-cratonic Indian continental lithosphere at deeper depths. By linking the extent of underthrusted lithosphere to a plate reconstruction model, Liu et al. (2024) constrained the timing of Indian cratonic underthrusting to 25-20 Ma. By applying a similar approach to the Arabia-Eurasia collision, we aim to quantify the amount of continental underthrusting and improve estimates of the timing of collision.

2 Data and Methods

2.1 Data

We selected 38 earthquakes that surround the Arabia-Eurasia collision zone (Figure 1a). We chose earthquakes with magnitudes between 5.5 and 7.2; earthquakes with $M_w > 5.5$ ensured that our data had good signal to noise ratio, whilst limiting magnitudes to $M_w < 7.2$ means that we avoided complications due to complex source mechanisms that are typical of large earthquakes. The earthquakes were also chosen to provide the broadest possible range of source locations, with the majority of events occuring along the western syntaxis of the Himalayan orogen, or in the Red Sea, Gulf of Aden, and Caucasus Mountains. An additional criteria is that the earthquakes were recorded by stations at regional ($10-30^\circ$) distances, at which the full waveform approach is particularly powerful (Tao et al., 2017). In total, the earthquakes were recorded by 1957 seismic stations from a number of permanent and temporary networks, which are listed in

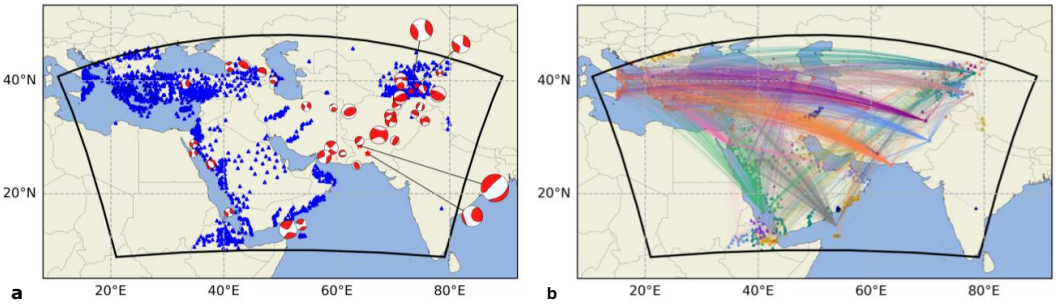


Figure 1. (a) Locations of earthquakes (red beachballs) and stations (blue triangles) used in this study. The focal mechanisms shown are those computed during our source inversions and are scaled by magnitude, ranging from M_w 5.3 – 7.2. (b) Raypaths between source and receivers for 10 representative earthquakes. The black box shows the boundary of our simulation region.

the Open Research section. Unfortunately this distribution of sources and receivers results in few north-south trending raypaths, due to a lack of data in Russia, Central Asia and the Indian Ocean and northeast Africa. However, combinations of NE-SW and SE-NW paths means that our dataset still provides relatively good crossing points beneath the region of interest (Figure 1b).

We preprocessed the raw seismic data by removing the mean, linear trend, and instrument response from each seismogram. We windowed the data and synthetics around the P, S, PP, SS, and surface wave arrivals, based on the predicted arrival times from the AK135 1D Earth model (Kennett et al., 1995), and applied a bandpass filter; we used corner frequencies of 15-100 seconds for body wave arrivals, and 25-100 seconds for short-period surface waves and 70-130 seconds for long-period surface waves (Liu et al., 2024). Using individual windows allowed us to ignore absolute amplitude differences between phases and periods, and also assign different weights to different seismic phases to maximize the improvement in the model.

2.2 Methods

To perform the full waveform inversion of mantle structure beneath the Middle East, we use the method of Tao et al. (2017). This method has been applied to East Asia (Tao et al., 2018), the Himalayas (Liu et al., 2024), and North America (Hua et al., 2025). The method is described in detail by Tao et al. (2018), and we provide an overview of the method below and in Figure S1.

Our general approach is to iteratively improve the fit of the full waveform between modelled and observed seismograms. We measure this misfit using a weighted normalized cross-correlation misfit, which can capture complexities in the waveforms of regional earthquakes that cross the mantle transition zone. We then calculate the gradient of the misfit and update the tomography model in this direction using the adjoint method (Tarantola, 1984; Tromp et al., 2005; Fichtner et al., 2006). Because both source and structure can affect the fit between data and synthetic seismograms, we inverted for both earthquake source parameters and mantle structure in alternating stages.

During the inversion, we first created synthetic seismograms using the wave propagation code `SPECFEM3D_GLOBE` (Komatitsch & Tromp, 2002a, 2002b). We then measured the misfit between the synthetics and the seismic data, using the weighted normalized cross-correlation misfit (Tao et al., 2017, 2018).

$$\chi = \sum_{s=1}^{N_s} \chi_s = \sum_{s=1}^{N_s} \sum_{i=1}^{N_{W,s}} W_s^i (1 - CC_s^i) \tag{1}$$

where the cross-correlation is given by:

$$CC_s^i = \frac{\int w_i^2(t) \mathbf{d}_s(t) \cdot \mathbf{u}_s(t)\, dt}{\sqrt{\int |w_i(t)\mathbf{d}_s(t)|^2 \cdot \int |w_i(t)\mathbf{u}_s(t)|^2\, dt}} \tag{2}$$

This equation measures how similar the modelled ($\mathbf{u}$) and observed ($\mathbf{d}$) waveforms are for each earthquake, s, and window, w_i. The weight parameter, W_i, is a function of the cross-correlation, maximum cross-correlation time shift and signal-to-noise ratio, as described by Liu et al. (2024). It is beneficial to use this misfit function when fitting regional waveforms as it can capture complexities in both phase and relative amplitude within each time window (Tao et al., 2017). In addition, it is insensitive to absolute amplitude differences between observed and synthetic data, allowing us to mitigate uncertainties associated with source magnitudes, radiation patterns, site effects and instrument errors (Tao et al., 2017).

The adjoint source is then used to simulate an adjoint wavefield, which is propagated back in time and correlated with the forward wavefield to obtain the misfit gradient (Tromp et al., 2005; Fichtner et al., 2006). For the first iteration, we updated the model in the direction of steepest descent ($\mathbf{d} = -\mathbf{g}$); for subsequent iterations, we used the preconditioned conjugate gradient method (Hestenes & Steifel, 1952; Fletcher & Reeves, 1964) to update the model in the direction that minimizes the data misfit, given by:

$$\mathbf{d}_i = -\mathbf{P}^{-1}\mathbf{g}_i + \gamma \mathbf{d}_{i-1} \tag{3}$$

where $\mathbf{d}$ is the updating direction, i is the iteration number, $\mathbf{P}$ is the preconditioner, $\mathbf{g}$ is the gradient of the misfit function and γ is the conjugate gradient update parameter. We smoothed the misfit gradient to regularize the inversion, using a Gaussian smoothing function with a horizontal half-width of 50 km and a vertical half-width of 25 km.

To ensure fastest convergence, the inverse Hessian should be used as the preconditioner. However, it is impracticable to directly calculate or invert the Hessian due to the prohibitively high computational cost. Therefore, we calculated an approximate Hessian, $\mathbf{H}$, by making a random perturbation, $\delta\mathbf{m}$, to the model, $\mathbf{m}$, and recomputing the gradient, $\mathbf{g}$:

$$\mathbf{H}\delta\mathbf{m} = \mathbf{g}(\mathbf{m} + \delta\mathbf{m}) - \mathbf{g}(\mathbf{m}) \tag{4}$$

Once the update direction, $\mathbf{d}$, was computed, we performed a line search in this direction to determine the optimum step length with which to update the model. This was done by perturbing the model by a small amount, ϵ, in the search direction to obtain a perturbed seismogram, $\delta\mathbf{u}$:

$$\delta\mathbf{u} = \mathbf{u}(\mathbf{m} + \epsilon\mathbf{d}) - \mathbf{u}(\mathbf{m}) \tag{5}$$

Then, assuming a linear relationship, any perturbed seismogram can be determined using the following equation:

$$\mathbf{u}(\mathbf{m} + \alpha\mathbf{d}) \approx \mathbf{u}(\mathbf{m}) + \alpha(\epsilon^{-1}\delta\mathbf{u}) \tag{6}$$

where α is the step length. In this study, we used a value of ϵ of 0.01, and determined the optimal step length α by performing a grid search of values between -1 and 2.

For the source inversion, we inverted for the earthquake's location, time and half duration and moment tensor. We obtained the initial sources from the Global Centroid Moment Tensor catalog (Dziewonski et al., 1981; Ekström et al., 2012), and updated the

source parameters using the method outlined above and in Tao et al. (2018). During the source inversion, we increased the weights fivefold for stations at $> 30°$ distance, as these teleseismic waveforms are less affected by mantle structure; this helps to reduce trade-offs between the inversion stages.

For the structure inversion, we inverted for Voigt-averaged V_P, V_S perturbations and three transverse isotropy (or "radial anisotropy") parameters: ϕ, ξ and η, following Tao et al. (2018) and Liu et al. (2024). ϕ and ξ describe the difference between horizontal and vertical P and S velocities, respectively, and η describes the anisotropy related to other angles of incidence, described by the elasticity tensor, C_{ijkl}.

$$V_P = \sqrt{\frac{V_{PV}^2 + 4V_{PH}^2}{5}} \tag{7}$$

$$V_S = \sqrt{\frac{2V_{SV}^2 + V_{SH}^2}{3}} \tag{8}$$

$$\phi = \frac{V_{PH}^2 - V_{PV}^2}{V_P^2} \tag{9}$$

$$\xi = \frac{V_{SH}^2 - V_{SV}^2}{V_S^2} \tag{10}$$

$$\eta = \frac{C_{1133}}{C_{1111} - C_{2323}} \tag{11}$$

We used S40RTS (Ritsema et al., 2011) as the starting model for V_S, with V_p given by the accompanying scaled model, P12 (Ritsema & van Heijst, 2002), and we use CRUST1.0 for the 3D crustal model (Laske et al., 2013). We set up the spectral element mesh using a single $60° \times 38°$ chunk, centered on 29° latitude and 50° longitude (Figure 1). We used 288 elements along the long axis of the cube, which corresponds to an average horizontal element size of ∼23.3 km at the surface. Based on prior benchmarking (Komatitsch & Tromp, 2002a, 2002b), this means that the simulation is accurate down to a period of ∼15 s.

3 Model Analysis

3.1 Statistical Metrics

Here, we discuss our model: Full Waveform Middle East 2024 (FWME24), and evaluate it against previous models. Compared with the starting model, FWME24 yields a better waveform and arrival time fit with the data for all seismogram components (Figure 2, Figures S2-4). This is particularly the case for S waves, which show slightly higher cross correlations and lower time shifts than P waves. Figure 3 breaks down the results for each iteration by phase. There was an initial decrease in fit for the first iteration, likely due to a combination of a large step length and use of the steepest descent direction for updating the model. There was a second decrease in cross correlation for Love waves, concurrent with a marked improvement in the S wave results, as the inversion sought to fit the higher weighted body waves for the T component of the seismograms (Figure 3a). However, by the end of the iteration, the Love wave results showed an overall improvement when compared with the starting model. In seismic tomography, there is always a trade-off between achieving the lowest data misfits without overfitting and overcomplicating the model. In addition to applying Gaussian smoothing – with a horizontal half-width of 50 km and a vertical half-width of 25 km – to the kernels during the inversion, we also calculated the root mean square (RMS) of the model values after each iteration, and compared this with the average cross correlation (Figure 3c). While the average cross correlation begins to flatten off during stage 2 of the inversion, the model

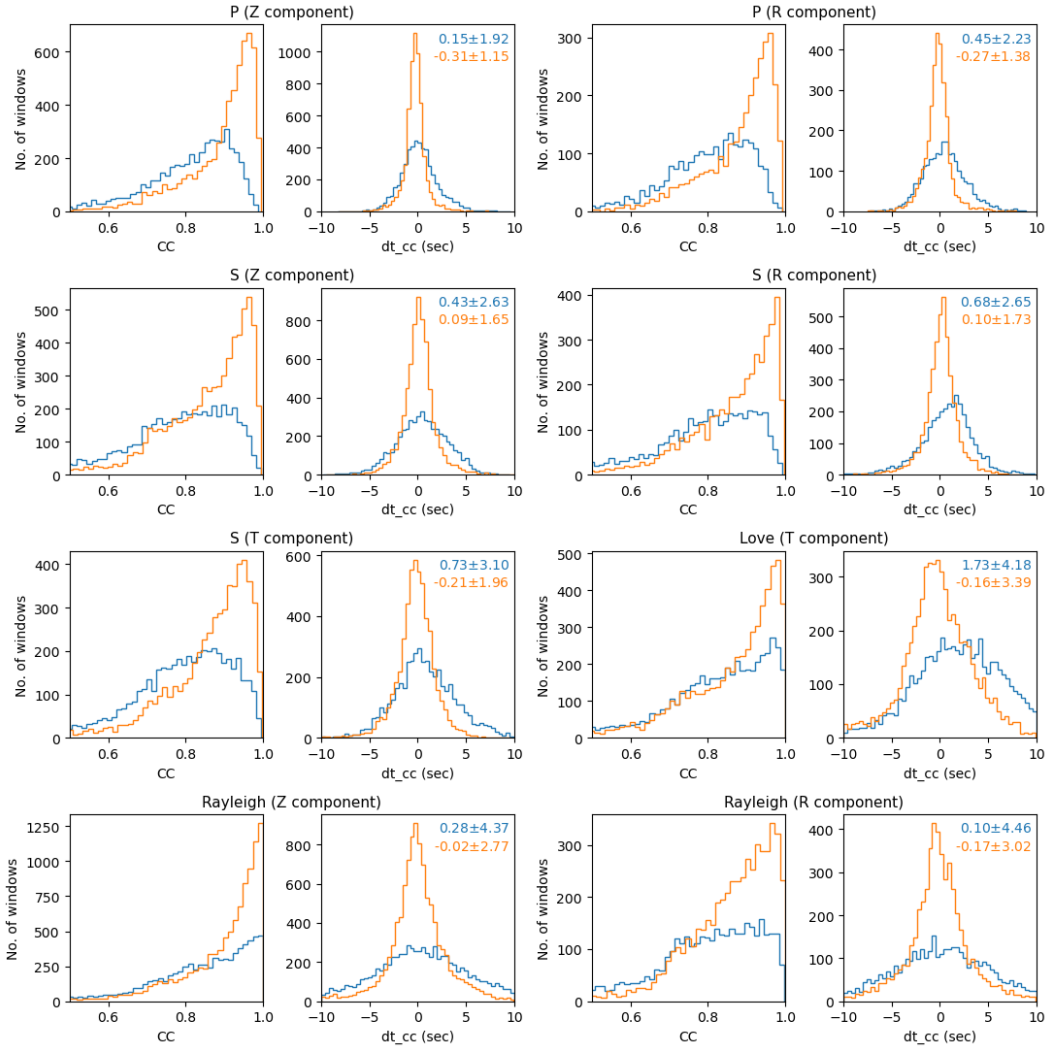


Figure 2. Histograms showing cross correlation and travel-time misfit for the starting model (blue) and our final model (orange) for different seismic phases. The mean and standard deviation of the travel-time misfit is specified in the top right of the plot for each phase.

RMS continues to increase, meaning that the model continues to get more complex without yielding significant improvements in the fit to the data. There were also only very minor visual changes to the model at this stage. Therefore, we terminated the inversion after 6 iterations in the second stage of the inversion. In total, we ran nine source iterations and nine structure iterations during stage one, and then three source iterations and six structure iterations in stage two.

3.2 Resolution Test

To assess the resolution of the model, we performed a point spread function test (e.g., Fichtner & van Leeuwen, 2015), a computationally-efficient method of assessing resolution of full-waveform inversions. We introduced Gaussian spherical anomalies of ±1% to our final model, spaced every 5 degrees horizontally and every 200 km vertically with a half-width of 40 km (Figure 4). We then created synthetic seismograms of the

In press at G-Cubed, September 2026, doi:10.1029/2026GC013003.

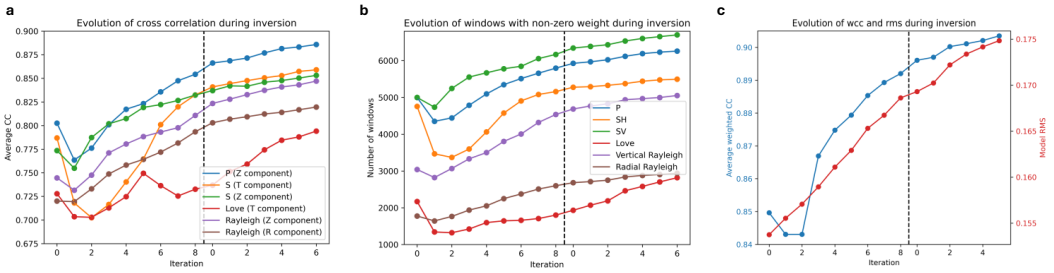


Figure 3. Evolution of cross correlation (a) and number of windows (b) per phase, along with the average cross correlation and model RMS (c) for each iteration. Dashed line denotes the division between stages 1 and 2, between which an additional source inversion was performed.

perturbed model using the same earthquakes and stations as used in the original inversion, for use in the resolution test.

We estimate the approximation of the resolution by the differences of the gradient of the perturbed model and model FWME24, which is related to the the Hessian acting on the model perturbation according to eq. (4). By applying the preconditioner, $\mathbf{P}$, calculated in the final iteration of the inversion to $\mathbf{H}\delta\mathbf{m}$, we can estimate the inversion's ability to recover the original model $\mathbf{m}$:

$$\mathbf{m} = (\mathbf{m} + \delta\mathbf{m}) - \mathbf{P}^{-1}\mathbf{H}\delta\mathbf{m} \tag{12}$$

Here, $\mathbf{P}^{-1}\mathbf{H}\delta\mathbf{m}$ is the resolution operator.

However, as this method only gives a conservative estimate of the true resolution, we performed a synthetic test with multiple iterations to improve the recovery of the model. This was done using the same inversion method as described in section 2.2, with the synthetic seismograms as the "data".

The results for the sythentic test after three iterations of the inversion are shown in Figures 4, S5 (V_S) and S6 (V_P). Due to the lack of stations in Africa and India, there is no resolution in this part of the model, which is outside of the region of interest; these regions are masked out in subsequent plots, using the same polygon for all wave types and depths for simplicity. However, there is good recovery of all point anomalies at 100 km depth across the Arabia-Eurasia collision zone. At 300 km and 500 km depth, there is good resolution beneath Eurasia. As most of the raypaths trend east-west, due to the lack of sources and stations in the north, there is some smearing in this direction. This may affect the shape of certain anomalies, but will not affect our estimates of collision timing as the convergence direction is orthogonal to this smearing. There is poorer recovery of point anomalies beneath central Arabia. At 300 km and 500 km depth, small amplitude, smeared points are recovered along the Red Sea and Saudi Arabia-Yemen border, due to the denser network of stations in these regions and in Afar (Figure 1); there is poorer resolution in central and eastern Arabia at these depths. At 700 km, there is better resolution towards the east of Arabia, where raypaths reach their deepest point before turning upwards and being recorded in Afar. However, the model generally has poor resolution for the lower mantle, especially towards the edges of the domain in western and southern Arabia and the Caucasus.

3.3 Model FWME24

Map plots of V_S anomalies, δV_S, for FWME24 are shown in Figure 5 and the vertical cross sections of the model through the collision zone in Figure 6. Different high

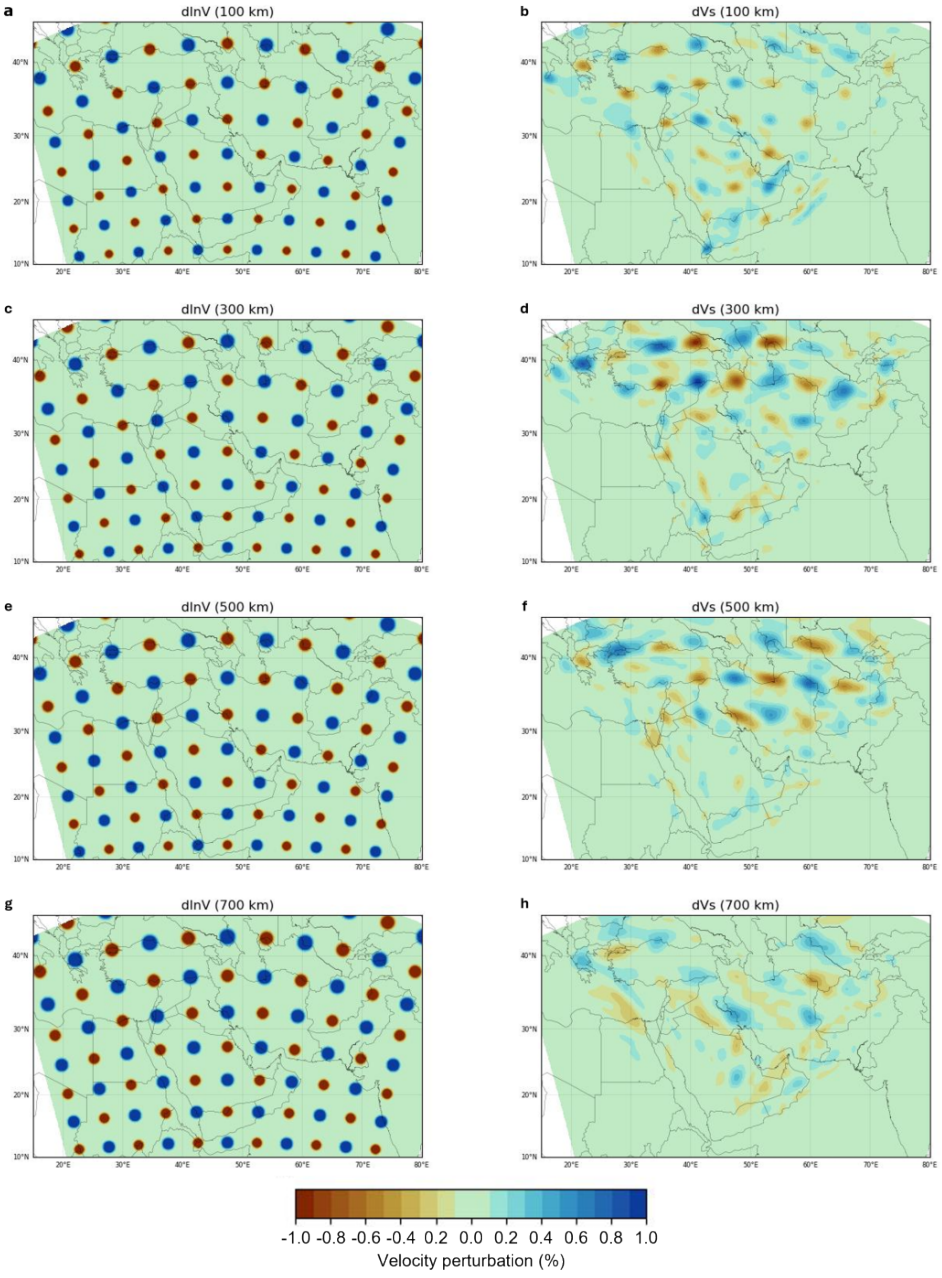


Figure 4. Input (a,c,e,g) and recovery (b,d,f,h) of Gaussian point heterogeneities, spaced every 200 km. Cross sections are shown in Figure S5.

velocity (HV), low velocity (LV) and slab (S) features are labelled in Figure 6 and discussed in section 4. Due to its better resolution, we primarily use our S wave model for interpretation and analysis; our P wave model and radial anisotropy results are shown in Figures S7 and S8, respectively.

Our model, FWME24, provides a much more detailed model of the mantle compared with the starting model S40RTS (Ritsema et al., 2011). This is likely due to our full waveform approach, where we can extract additional information from triplicated waves (Tao et al., 2017), and regional focus. For these reasons our model more closely resembles other full waveform models (e.g., REVEAL, Thrastarson et al., 2024) and regional models (e.g., MESWA, Rodgers et al., 2024). However, our approach images finer scale features than these other models, allowing for more detailed tectonic interpretation. Our resolution test demonstrates that such small scale features can be well resolved at least down to 500 km beneath the Turkish-Iranian plateau, and also across Arabia at shallower depths.

Strong (∼5%) slow δV_S anomalies are present under the Afar region at all depths, but additionally follow a northward trend along western Arabia before diverting east and west to form a "T shape" beneath the Turkish-Iranian plateau, at shallow depths of 100 and 200 km (Figure 5). These features, likely related to the Afar plume, match those shown in other S wave models (Auer et al., 2014; Ritsema et al., 2011; Rodgers et al., 2024; Schaeffer & Lebedev, 2013; Thrastarson et al., 2024). Our V_P results also show this feature (Figure S7), matching other regional and global P wave models including UU-P07 (Amaru, 2007) and MEPT (Bozdağ et al., 2025). There also appears to be an additional upwelling beneath Makran (LV2 features, Figure 6), which may be further interacting with the Afar plume beneath Iran.

Other features at 100 and 200 km depths include the general shape of the seismically fast anomaly beneath Arabia and the Zagros mountains, which likely represents cratonic Arabian continental lithosphere due to its $\sim$ 250 km thickness. This feature extends northward beyond the current plate boundary (orange lines in Figure 5), indicating that there has been some degree of underthrusting as the Arabian plate moves northwards.

At greater depths (400 and 600 km), FWME24 shows a more complex pattern of P and S wave velocity anomalies, with additional detail when compared with previous models (Figure 5). Although some cross sections appear to show linear, dipping fast anomalies (S1-3 features, Figure 6), there is generally a lack of a clear subducted slab beneath the Arabia-Eurasia collision zone (HV1 features, Figure 6). This indicates that there has been a complex history of subduction and collision, with slab break-off occurring at different times during a diachronous collision (e.g., Kaviani et al., 2018; Veisi et al., 2021). Some of these spherical-shaped fast anomalies could represent subducted Arabian passive margin lithosphere, given their similarity to features beneath the Himalayas which were interpreted by Liu et al. (2024) as subducted non-cratonic Indian lithosphere.

Overall, challenges due to limited data availability notwithstanding, model FWME24 gives a detailed image of the upper mantle structure beneath the Arabia-Eurasia collision. This can be used to improve our understanding of the tectonic history of the region, as discussed in the following section.

4 Discussion

4.1 Timing of Arabia-Eurasia Collision

As discussed in section 3, there is a region with fast seismic wavespeeds down to ∼250 km beneath Arabia, which also extends beneath the Zagros mountains into central Iran (Figures 5 and 6). These thick and strong δV_S anomalies (+5% and higher) are

In press at G-Cubed, September 2026, doi:10.1029/2026GC013003.

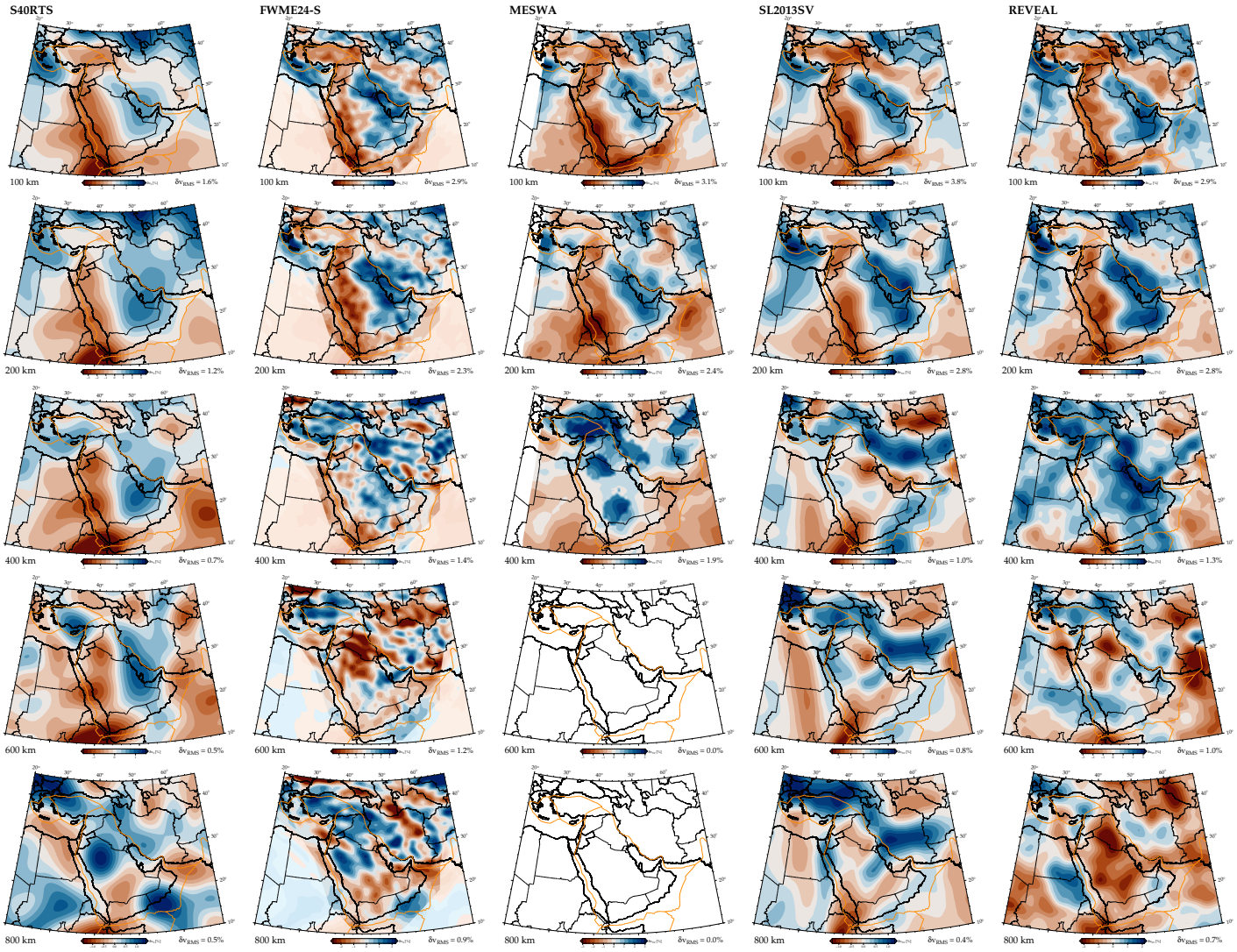


Figure 5. Maps of fast (blue) and slow (red) velocity anomalies, δV_S, at different depths for five different models: S40RTS (starting model, Ritsema et al., 2011), FWME24-S (this study), MESWA (Rodgers et al., 2024, crust and upper mantle only), SL2013SV (Schaeffer & Lebedev, 2013), REVEAL (Thrastarson et al., 2024). For FWME24, regions with no resolution (i.e., Africa and the Indian Ocean) are masked and shown only faintly based on a depth-independent polygon inferred from the resolution test (Figure 4). Note that the colour scale varies in each panel depending on the model RMS.

In press at G-Cubed, September 2026, doi:10.1029/2026GC013003.

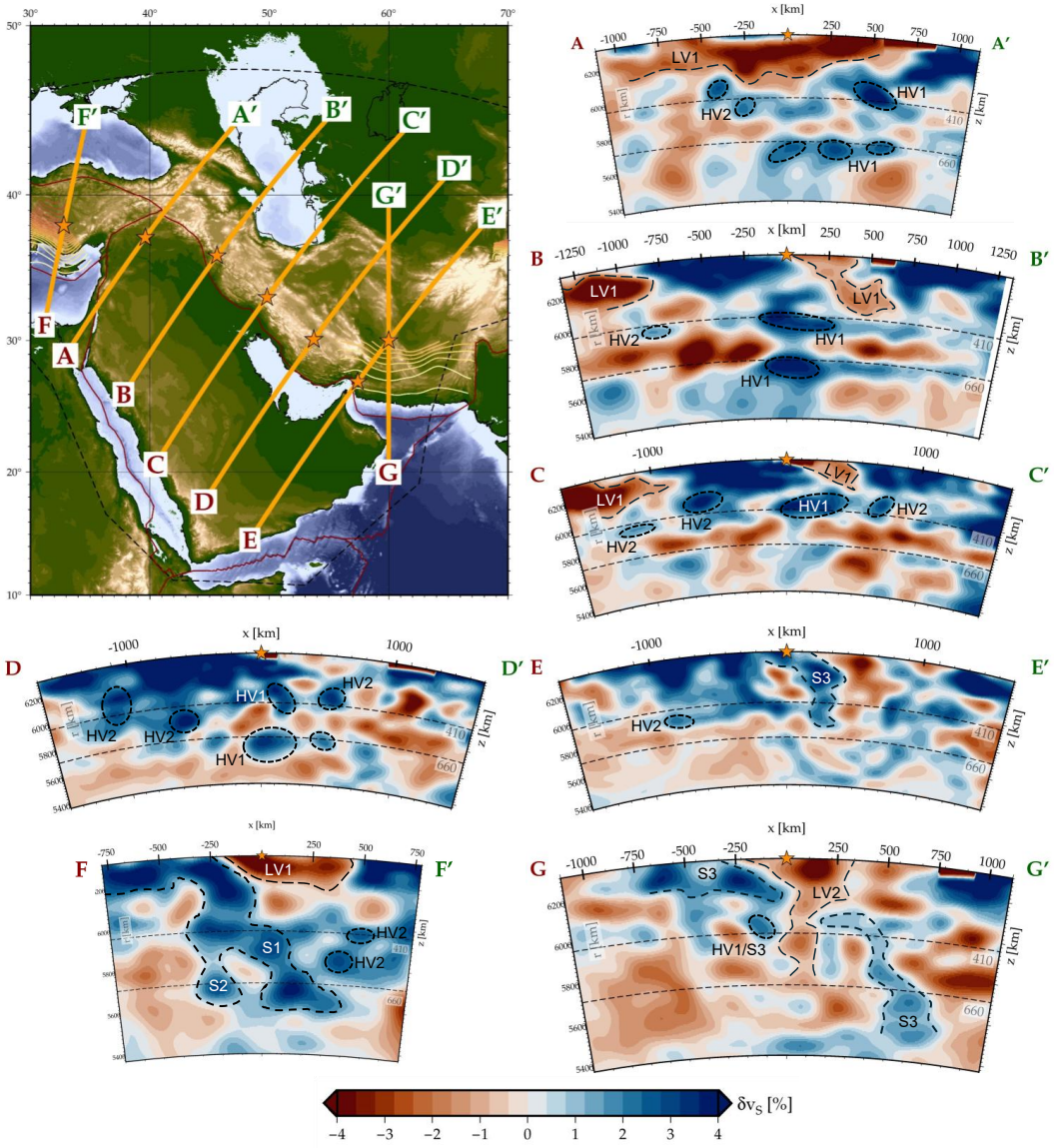


Figure 6. Cross sections of mantle structure across the Arabia-Eurasia collision, according to model FWME24-S. HV, S and LV labels indicate features that are discussed in section 4. Profiles are plotted perpendicular to the Arabia-Eurasia plate boundary (red line).

In press at G-Cubed, September 2026, doi:10.1029/2026GC013003.

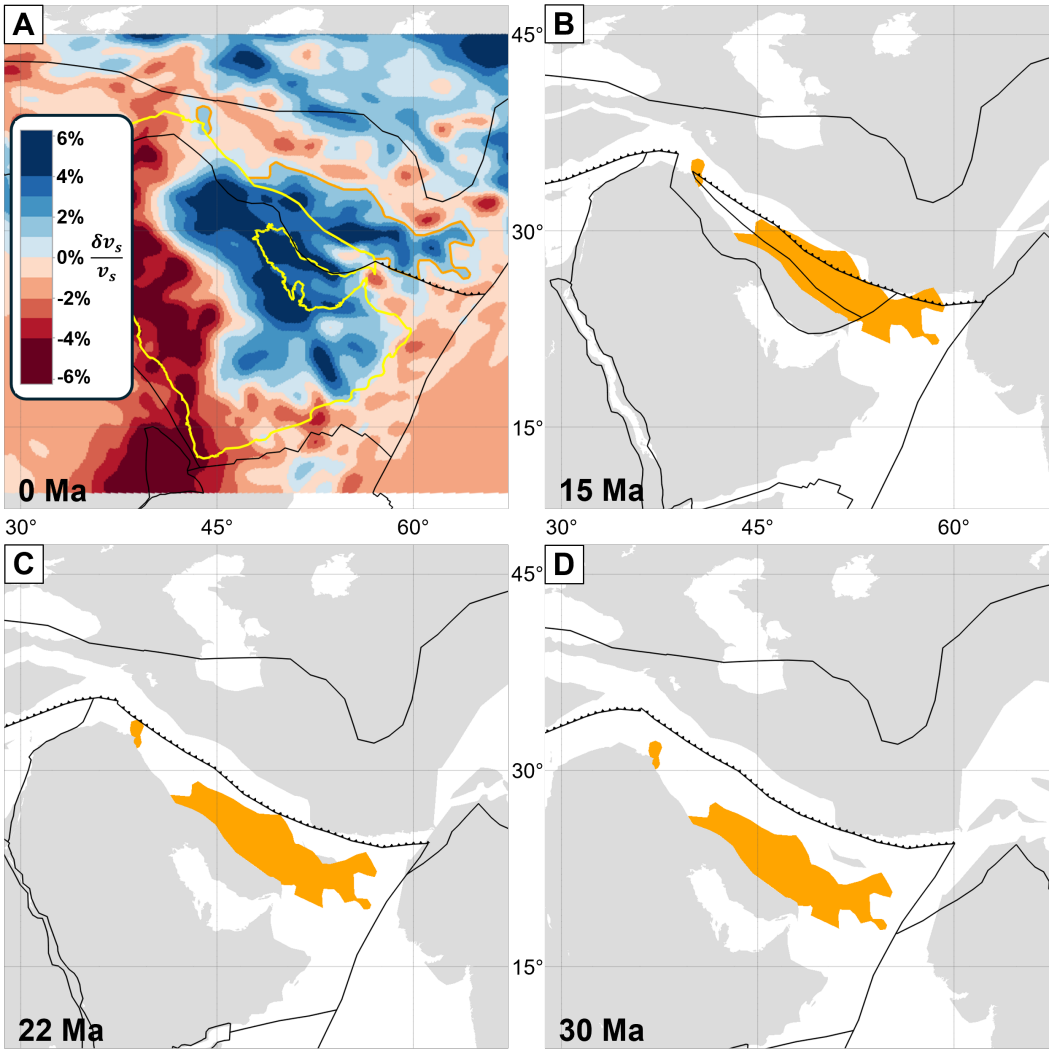


Figure 7. Reconstruction of the Arabian continent that has underthrusted Eurasia. (a) Plate reconstruction at 0 Ma underlain by δV_S anomalies at 200 km depth. Fast anomalies greater than 1% on the northern side of the Zagros suture (i.e. Arabian plate, yellow) are contoured in orange. (b-d) Underthrusted Arabia (orange) is reconstructed back in time in a mantle reference frame using the model of Müller et al. (2019).

indicative of cratonic continental lithosphere, and so we interpret this as Arabian lithosphere that has underthrusted Eurasia to the north (cf. Liu et al., 2024).

To constrain the edge of the Arabian lithosphere, we contoured the edge of the +1% δV_S anomaly in the 200 km depth slice (Figure 7a). We then reconstructed the position of this lithosphere through time using the Arabian plate motion modelled by Müller et al. (2019). This plate reconstruction is in a mantle reference frame (Tetley et al., 2019), and also attempts to restore deformation in the upper plate (after McQuarrie & van Hinsbergen, 2013), resulting in a more accurate trench location when compared with rigid plate models (e.g., Seton et al., 2012).

Our reconstruction of underthrusted Arabian lithosphere is shown in Figure 7. The first point where the Arabian lithosphere encounters the Tethyan subduction zone is at

22 Ma (Figure 7c), and more of the lithosphere progressively encounters the trench until 15 Ma (Figures 7b). This would indicate that underthrusting of thick Arabian lithosphere, or hard collision, occurred diachronously from 22-15 Ma. This seismologically-constrained timing matches the timing of hard collision constrained with changes in sediment provenance, depositional environment and exhumation rates (Ballato et al., 2011). It would also explain the cessation of magmatism which occurred progressively from 22 Ma in the northwest part of the Urumieh–Dokhtar magmatic arc to 16 Ma in the central region of the arc (Chiu et al., 2013). However, magmatism continued in the southeast of the arc until 10-6 Ma – this is inconsistent with the 22 Ma collision time shown in Figure 7c, but could reflect a lag-time for cessation of magmatism following continental collision, or uncertainties in identification of the edge Arabian lithosphere or reconstructed position of the plate boundary.

There are uncertainties associated with the identification of underthrusted lithosphere, and choices of different depth slices or higher δV_S anomaly contours will affect the results. In the analysis of Liu et al. (2024), a δV_S +5% contour was chosen, which in our case would significantly delay the collision time to 9 Ma. Given that the mantle is hotter overall in this region due to the Afar plume (e.g., Figure 5), the mean V_S value is likely to be lower at 200 km, which would affect the δV_S contours. δV_S amplitudes will also be affected by inversion choices and data coverage. Thus, a +1% contour appears to be a reasonable choice for the boundary of Arabian lithosphere. However, using a higher value would shorten the lithosphere by ∼50 km for each percentage, resulting in a collision time that would be ∼2 Myrs later per percent. Similarly, using a different depth also affects the results, with δV_S +1% contours at 150 and 250 km depth predicting collision times of 17-11 Ma and 25-13 Ma, respectively (Figure S9). Thus, our results support a Miocene Arabia-Eurasia collision regardless of the choice of depth slice or velocity contour. This timing is in agreement with several other estimates for the Arabia-Eurasia collision, including from studies of exhumation, foreland basin formation, and faunal exchange (Ballato et al., 2011; Fakhari et al., 2008; Rögl, 1999; Harzhauser et al., 2007).

4.2 Final Neotethys Subduction

A Miocene age for the Arabia-Eurasia collision means that earlier events such as the slowdown of the Arabian plate at 35-30 Ma (Jolivet & Faccenna, 2000) and transition from extensional to contractional deformation (Ballato et al., 2011) must be explained by other mechanisms. One theory is that these events were caused by the end of subduction of Neotethys oceanic crust, resulting in a soft collision as thinned Arabian continental crust arrived at the subduction zone (Ballato et al., 2011). Our ∼22 Ma age for cratonic Arabia-Eurasia collision predicts that there was a ∼8-13 Ma period where thinned continental lithosphere was subducting into the mantle, which should be identifiable to seismic tomography.

An analogy to this setting could be provided by the India-Eurasia collision, which has been ongoing for ∼60 Myrs. In their seismic tomography model, Liu et al. (2024) did not image any clear slabs beneath Tibet, in contrast to linear slabs imaged beneath East Asia, the Phillipines and Sumatra. Instead, they imaged fragmented, spherical-shaped high velocity anomalies down to 600 km. These were interpreted to result from subduction and break off of continental lithosphere, which would have accommodated the convergence between thin Greater India continental lithosphere and Tibet.

In our cross sections through the Arabia-Eurasia collision belt (Figure 6, profiles A-E), we also do not image coherent slabs, suggesting a complex history of slab break off in the region (cf. Kaviani et al., 2018). The isolated, spherical geometry of some of these high velocity regions - and similarity to the model of Liu et al. (2024) - indicates that there has been a period of continental subduction beneath Eurasia. This would be consistent with a two-stage collision model where an initial soft collision, and continu-

ing subduction, of non-cratonic lithosphere was followed by a hard collision of cratonic Arabia (e.g., Ballato et al., 2011; Darin & Umhoefer, 2022).

Alternatively, these small fast anomalies could instead represent lithospheric drips from the overriding plate, as suggested by previous seismic tomography studies of the region (Portner et al., 2018; Kounoudis et al., 2020). Geodynamic models of small-scale drips in Anatolia are consistent with seismic data and can also explain the enigmatic uplift of the Anatolian plateau (Göğüş et al., 2017). Lithospheric delamination could also explain fragmented anomalies in other parts of our model, and we further discuss mechanisms for this process in section 4.3.

To both the east and west of this region, there is active subduction ongoing at the Hellenic and Makran subduction zones. Here, we image more linear and coherent fast anomalies that more closely resemble a traditional slab (S1, Figure 6). However, there is still some interesting complexity in both of these regions.

Beneath Cyprus and Anatolia, we image a single slab down to the top of the mantle transition zone. However, two parallel high velocity anomalies are imaged at deeper depths (S1 and S2, Figure 6). This could be a result of fragmentation and detachment of the Cyprian slab at depth, which has been suggested to be occurring based on previous seismic tomography images of the region (Biryol et al., 2011), which would also explain the variation in V_S amplitude along the slab. However, our model does show slab S1 penetrating the lower mantle, in contrast to the findings of Biryol et al. (2011). An alternative explanation could be that slabs S1 and S2 represent two different phases of subduction, with one being Mediterranean oceanic lithosphere and the being Neotethyan oceanic lithosphere. While subduction of the Mediterranean ocean is active today, the Neotethys ocean would have been consumed by ∼60 Ma in this region when the Taurides collided with the Pontides (Gürer & van Hinsbergen, 2019). This slab would be expected to be at least 600 km deep based on slab sinking rates of 1-2 mm/yr (e.g., Hafkenscheid et al., 2006), which is consistent with the depths of S1 and S2.

At the eastern end of our region, we image a shallowly-dipping Makran slab (S3, Figure 6). We also image a vertical slow anomaly (LV2, Figure 6) that might be associated with an upwelling plume, an interpretation that is supported by mantle transition zone thickness variations (Kaviani et al., 2018). Interestingly, the presumed hot upwelling (LV2) appears to break through the slab (Profile G, Figure 6). Mantle plumes are expected to interact with slabs, and this appears to be reflected in tomographic model structure inSouth America (Portner et al., 2017) and the Afar-Aegean system (Faccenna et al., 2013), for example. During such interactions, plumes may play a more active role in modifying subduction dynamics than previously recognized (Heilman & Becker, 2022), and the Makran subduction zone might be another region where there is active plume-slab interaction.

4.3 Lithospheric Delamination

Figure 6 illustrates major areas of slow seismic wavespeeds at shallow depths (LV1), which we interpret as evidence of northward flow of the Afar plume. Beneath many of these low velocity regions, there are isolated fast velocity anomalies in the mantle transition zone (HV2), which in some cases are hundreds of kilometers away from the location of the former Neotethyan subduction zone (Müller et al., 2019) and thus are unlikely to represent subducted material (i.e. HV1 features). An alternative mechanism to explain these features is required, with a key candidate being lithospheric delamination.

In the well-resolved northern half of our model region, we observe an E-W trending region of hot material that likely originated from the Afar plume (Figure 5). We suggest that the northward flow of the Afar plume has led to erosion and delamination of significant portions of Eurasian and Arabian lithosphere (e.g., Camp & Roobol, 1992).

In press at G-Cubed, September 2026, doi:10.1029/2026GC013003.

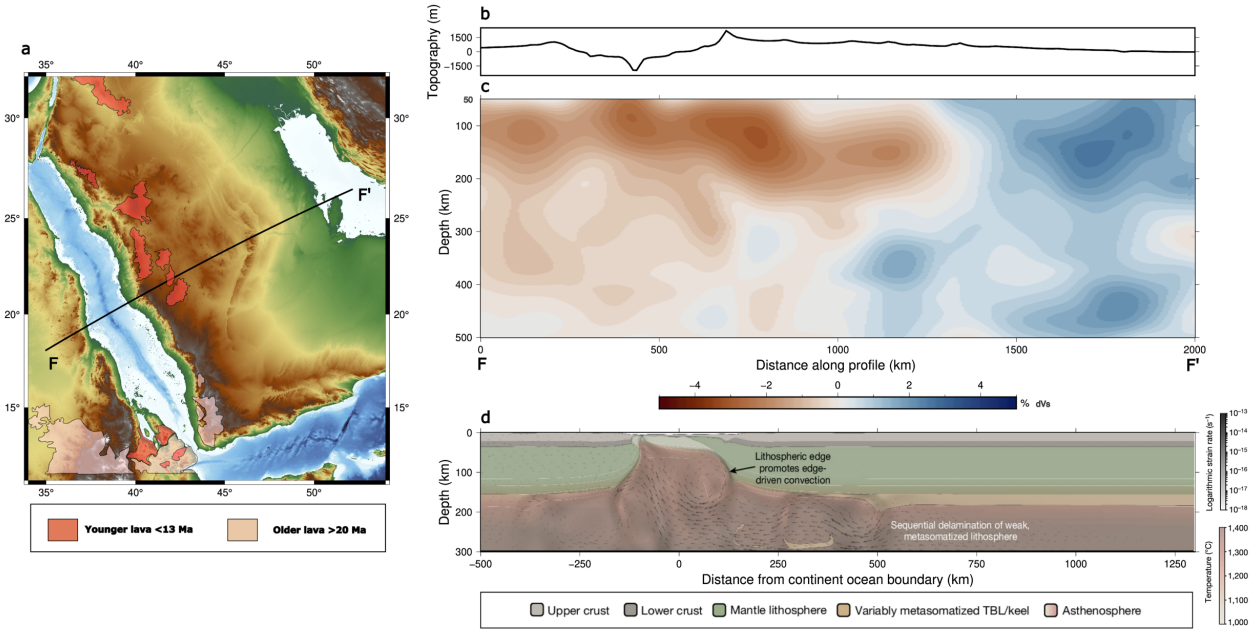


Figure 8. Evidence for rift-induced lithospheric delamination in Arabia. (a) Map of the Red Sea and Arabia, showing the location of young volcanics along with profile F-F'. (b) Topography along F-F'. (c) δV_S along F-F' from model FWME24. (d) Geodynamic model 30 Myrs after rift initiation from Gernon et al. (2023, 2024).

An additional cause of lithospheric delamination beneath the Turkish-Iranian plateau could be convective removal following continental collision and thickening (e.g., Li et al., 2016; Liu et al., 2024), which could have facilitated further flow of plume material.

We note that the southern half of our model region - beneath Arabia - is not as well resolved as further north. However, our resolution test (Figure 4) does show some recovery of the point heterogeneities inputted in this region, and so we will discuss possible origins for these features. As in Eurasia, a possible cause of lithospheric delamination could include erosion due to a northward-migrating Afar plume (e.g., Camp & Roobol, 1992). The volcanic fields of Harrat Rahat (10 Ma), Harrat Khaybarat (5 Ma) and Harrat Ithnayn (3 Ma) record a clear northward age-progressive trend (Camp & Roobol, 1992; Stern & Johnson, 2010), which has been interpreted to be the result of northward migration of plume material along the western margin of Arabia (Camp & Roobol, 1992). Our model is consistent with this hypothesis given the broad low velocity anomalies beneath western Arabia.

An alternative driver of delamination of Arabian lithosphere is edge-driven convection at the Red sea margin. A recent geodynamic model by Gernon et al. (2023) showed that rifting of the lithosphere and steepening of the lithospheric-asthenospheric boundary can cause convective instabilities that propagate away from the rift axis, progressively removing the thermal boundary layer at the base of the lithosphere. Gernon et al. (2023) calculated that these instabilities migrate at approximately 15-20 km/Myr; given that Red Sea rifting started at ~30-25 Ma (Joffe & Garfunkel, 1987), lithospheric delamination would be expected to be currently occurring ~300-600 km from the Red Sea. This is consistent with the geometry of the seismically fast regions shown in FWME24 (Figure 8b.

In press at G-Cubed, September 2026, doi:10.1029/2026GC013003.

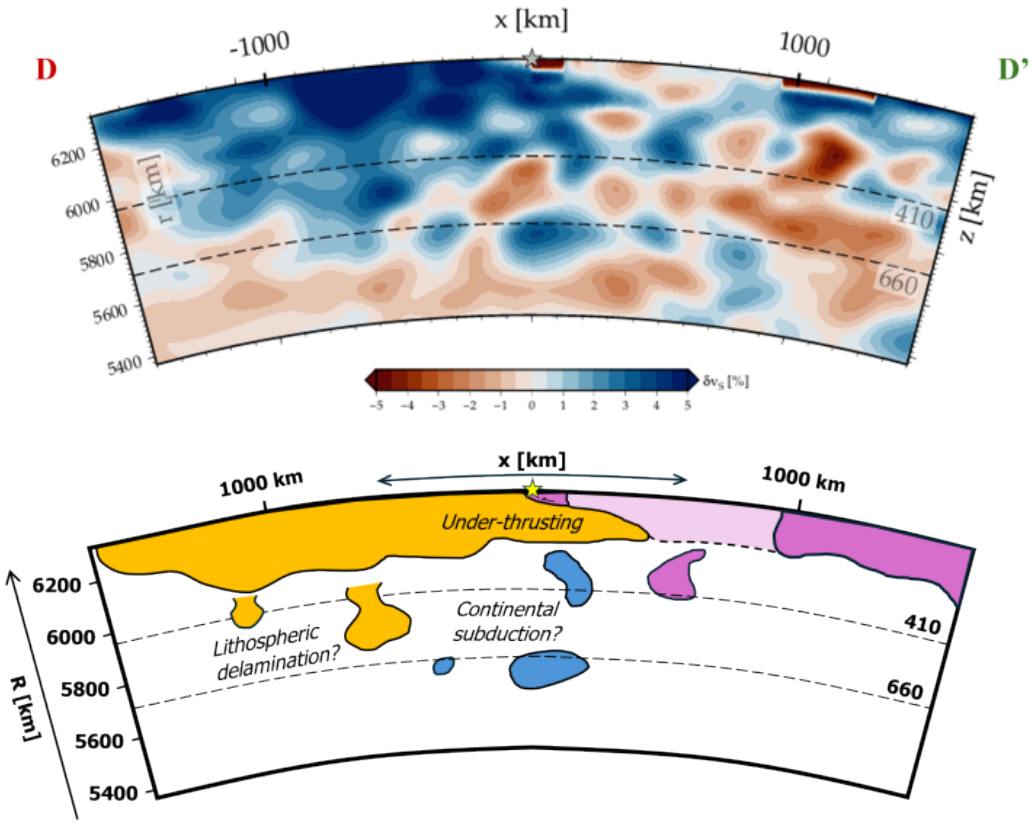


Figure 9. Interpretation of tomographic cross section D-D' across the Arabia-Eurasia collision zone, showing underthrusting of Arabia beneath Eurasia, deeper structures related to subduction of thin continental lithosphere and potential lithospheric delamination. Location of the cross section D-D' is shown in Figure 6.

The main line of evidence used by Gernon et al. (2023) to support their model came from the spatio-temporal link between rifting and kimberlite volcanism. Although no kimberlite fields have been found in Saudi Arabia, there has been recent (<10 Ma) volcanism that has erupted garnet-bearing xenoliths that indicate that melting occurred >100 km deep (McGuire, 1988). In addition, the youngest volcanics are furthest from the rift axis (Stern & Johnson, 2010), consistent with the expected trend if these melts are related to upwelling return flow from lithospheric delamination (Gernon et al., 2023). This could provide independent evidence that rift-induced delamination is occurring in Arabia, and thus model FWME24 could provide seismological support for this process to complement the geodynamic modelling and geochemical data.

4.4 Synthesis

A general interpretation of the mantle structure is shown in Figure 9. This summarizes the different features identified and discussed above, including cratonic underthrusting, continental subduction and lithospheric delamination.

We interpret fragmented fast δV_S anomalies beneath the collision zone as subducted continental lithosphere, which would support an earlier soft collision of Arabian passive margin prior to arrival of cratonic lithosphere (e.g., Ballato et al., 2011; Darin & Umhoefer, 2022). We also identify Arabian cratonic lithosphere that has underthrusted Eura-

sia. By reconstructing the motion of Arabia, we estimate that cratonic Arabia first collided with Eurasia at 22 Ma (Figure 7). This timing is in agreement with a number of geological constraints (e.g., Ballato et al., 2011; Fakhari et al., 2008; Rögl, 1999; Harzhauser et al., 2007), and indicates that earlier deformation events recorded in the structural geology and sedimentary record instead record a change in subduction style and not a transition from subduction to collision.

Lithospheric delamination appears to be occurring beneath both Arabia and Eurasia (Figure 9), based on our interpretation of high velocity anomalies away from the former Neotethys subduction zone. Potential mechanisms for this process include convective instabilities driven by Red Sea rifting (e.g., Gernon et al., 2023), which could explain the tomographic results for Arabia as well as deep-sourced volcanism along the Red Sea margin (e.g., McGuire, 1988), or delamination due to the northward flow of the Afar plume (Camp & Roobol, 1992). Eurasian lithosphere could also have been removed due to Afar plume activity (e.g., Figure 5), or by convective removal following continental collision and thickening (e.g., Li et al., 2016; Liu et al., 2024).

5 Conclusions

We apply full waveform inversion to image the mantle structure beneath the Arabia-Eurasia collision zone. Making use of a normalized cross-correlation misfit function, we produced a new seismic tomography model for the upper mantle beneath Eurasia and Arabia.

Our model, FWME24, provides a detailed image of the upper mantle, allowing us to better understand the recent history of the Arabia-Eurasia collision. Fragmented high velocity anomalies indicate a complex history of slab break off, which we suggest is related to a period of continental subduction following a soft collision. By integrating our seismic tomography model with plate reconstructions, we estimate that a hard collision between cratonic Arabia and Eurasia initiated at ∼22 Ma.

Our imaging and interpretation of features in our model FWME24 highlights how a four-dimensional analysis of the Arabia-Eurasia collision is important for understanding the tectonic history of the region. This complements geological analysis at the surface, helping to provide a larger-scale overview of the tectonics of the region. We suggest that this method could be important in understanding the tectonic history of other recent collisional belts.

6 Availability Statement

The `SPECFEM3D_GLOBE` software (Komatitsch & Tromp, 2002a, 2002b) used to perform the waveform simulation is open-source and available at `specfem.org`. Data processing and misfit measurement was carried out using ObsPy (`obspy.org`, Beyreuther et al., 2010). Waveform and station data were downloaded from the IRIS Data Management Centre, with the exception of data from the Saudi National Seismic Network which was accessed from KAUST. The networks used were: 1E (Pelletier et al., 2018), 1J (Moretti et al., 2021), 1N (Malet et al., 2015), 2H (Keir & Hammond, 2009), 3K (Bastow et al., 2016), 4B (*TASK FORCE KIRGISTAN*, 2008), 4H (Hammond et al., 2011b), 5C (Schurr et al., 2012), 5H (Hammond et al., 2011a), 5H (Weidle et al., 2013), 6C (Helffrich, 2006), 6C (Haberland et al., 2009), 6E (*Nisyros network*, 2007), 7B (Yuan et al., 2008), 7C (Vergne et al., 2014), 7C (Costanzo et al., 2022), 7L (Eibl et al., 2020), 8H (Yuan et al., 2017), 8X (AlpArray Seismic Network , 2016), 9H (Schurr et al., 2017), A2 (NAS RA, 2022), AB (Azerbaijan National Academy of Sciences, 2003), AC (Polytechnic University of Tirana, 2002), AF (Penn State University, 2004), BA (*UniBAS*, 2005), BS (BAS, 1980), BW (University of Munchen, 2001), CB (IGPCEA, 2000), CK (CAREMON, 2009), CL (Corinth Rift Laboratory Team & Epos-France, 2013), CQ (Geological Survey Department Cyprus, 2013),

CR (University of Zagreb, 2001), CZ (Charles University in Prague et al., 1973), G (IPGP & EOST, 1982), GE (GEOFON Data Centre, 1993), GO (Ilia State University, 1988), GR (BGR, 1976), HA (University of Athens, 2008), HC (Technological Educational Institute of Crete, 2006), HL (National Observatory of Athens, 1975), HP (University of Patras, 2000), HT (Aristotle University of Thessaloniki, 1981), HU (Kövesligethy Radó Seismological Observatory, 1992), IB (Geosciences Barcelona & Institute Earth Sciences "Jaume Almera", 2007), II (EarthScope Consortium, 1986), IM (Various Institutions, 1965), IS (*Israel Seismic Network*, 1982), IU (Albuquerque Seismological Laboratory/USGS, 1988), IV (INGV, 2005), IY (Calabria, 1981), KC (CAIAG, 2008), KN (KIS & UC San Diego, 1991), KO (Boğaziçi University, 1971), KR (KIS, 2007), KW (*Kuwait National Seismic Network*, 1997), KZ (KNDC, 1994), MD (Geological and Seismological Institute of Moldova, 2007), ME (IHMS, 1982), MN (MedNet, 1990), MP (SLUB & LSDAUoB, 2014), MT (OIMV, 2006), OE (ZAMG, 1987), OT (University of Bari "Aldo Moro", 2013), PF (OVPF & IPGP, 2008), PL (Polish Academy of Sciences, n.d.), QZ (SEME, 2003), RO (National Institute for Earth Physics, 1994), SA (Endo et al., 2007), SG (Multiple Operators, 1997), SI (*Province Südtirol*, 2006), SK (ESI SAS, 2004), TJ (National Academy of sciences of Tajikistan, 2009), TU (Disaster and Emergency Management Authority, 1990), TV (INGV, 2008), WI (IPGP, 2008), X7 (Chevrot et al., 2017), XA (Sandvol et al., 2017), XE (Chiarabba et al., 2022), XK (INGV, 2020), XW (Paul et al., 2007), XW (Leroy et al., 2009), XY (Paul et al., 2013), XZ (Leroy, 2003), Y2 (Roecker & Levin, 2007), Y5 (Obermann et al., 2022), Y9 (Sobiesiak & Schurr, 2007), YB (Paul et al., 2000), YB (Sandvol, 2013), YD (University of Leeds, 2009), YF (van der Lee et al., 1999), YG (University of Leeds, 2005), YH (DANA, 2012), YI (Paul et al., 2008), YL (Mackey, 2021), YQ (Keir et al., 2017), YR (Levèque & RESIF, 2010), YR (ISTerre, 2005), YR (Metaxian et al., 2018), YU (Harjes, 1996), YY (Keranen, 2013), YZ (Royal Holloway, University of London, 2005), YZ (Passarelli et al., 2017), Z3 (Friederich & Meier, 2005), Z3 (AlpArray Seismic Network, 2015), Z4 (Asch et al., 2006), ZE (Ebinger, 2007), ZF (University of Bristol, 2007), ZF (Fontaine et al., 2015), ZH (Paul et al., 2006), ZI (Barruol, 2007), ZK (Gao, 2009), ZR (GEOFON, 2000), and ZZ (Meier et al., 2004). Centroid moment tensors were accessed from `globalcmt.org`.

Acknowledgments

We thank editor Anne Paul and two anonymous reviewers for their comments and editorial handling which helped to improve this manuscript from an earlier version. We thank P. Martin Mai and Armando Espinola Cardona for providing data from the Saudi National Seimic Network for 10 events. E.J.C. acknowledges funding from a Ewing-Worzel Fellowship from the University of Texas Institute for Geophysics and a Muehlberger Fellowship from the Jackson School of Geosciences, University of Texas at Austin. C.L. and S.P.G. were supported by NSF grant EAR1838444. Partial support for E.J.C. and T.W.B. came from NSF grant EAR1925939.

Conflict of Interest Statement

The authors declare there are no conflicts of interest for this manuscript.

References

Alavi, M. (1994). Tectonics of the zagros orogenic belt of iran: new data and interpretations. *Tectonophysics*, *229*(3-4), 211–238. doi: 10.1016/0040-1951(94)90030-2

Albuquerque Seismological Laboratory/USGS. (1988). *Global seismograph network (gsn - iris/usgs).* International Federation of Digital Seismograph Networks. Retrieved from `https://www.fdsn.org/networks/detail/IU/` doi: 10.7914/SN/IU

AlpArray Seismic Network . (2016). *Central adriatic seismic experiment (case) - alparray.* AlpArray Working Group. Retrieved from http://networks.seismo.ethz.ch/networks/8x/ doi: 10.12686/ALPARRAY/8X_2016

AlpArray Seismic Network. (2015). *Alparray seismic network (aasn) temporary component.* AlpArray Working Group. Retrieved from http://networks.seismo.ethz.ch/networks/z3/ doi: 10.12686/ALPARRAY/Z3_2015

Amaru, M. L. (2007). *Global travel time tomography with 3-D reference models* (Ph.D. Thesis (Vol. 274)). Utrecht University.

Aristotle University of Thessaloniki. (1981). *Hellenic unified seismological network.* International Federation of Digital Seismograph Networks. Retrieved from https://www.fdsn.org/networks/detail/HT/ doi: 10.7914/SN/HT

Asch, G., Mohsen, A., Bräuer, B., Hofstetter, R., Jaser, D., El-Kelani, R., & Weber, M. (2006). *Desire - seismology (2006/2008).* GFZ Data Services. Retrieved from http://geofon.gfz.de/doi/network/Z4/2006 doi: 10.14470/M97551339354

Auer, L., Boschi, L., Becker, T. W., Nissen-Meyer, T., & Giardini, D. (2014). Savani: A variable resolution whole-mantle model of anisotropic shear velocity variations based on multiple data sets. , *119*(4), 3006–3034. Retrieved 2026-07-22, from https://onlinelibrary.wiley.com/doi/abs/10.1002/2013JB010773 (_eprint: https://agupubs.onlinelibrary.wiley.com/doi/pdf/10.1002/2013JB010773) doi: 10.1002/2013JB010773

Azerbaijan National Academy of Sciences, Republican Seismic Survey Center. (2003). *National seismic network of azerbaijan.* FDSN network code AB (2003–present); no DOI registered, see https://www.fdsn.org/networks/. International Federation of Digital Seismograph Networks.

Ballato, P., Uba, C. E., Landgraf, A., Strecker, M. R., Sudo, M., Stockli, D. F., ... Tabatabaei, S. H. (2011). Arabia-Eurasia continental collision: Insights from late Tertiary foreland-basin evolution in the Alborz Mountains, Northern Iran. *Bulletin of the Geological Society of America*, *123*(1-2), 106–131. doi: 10.1130/B30091.1

Barruol, G. (2007). *Plume - polynesia lithosphere and upper mantle experiment, 2001-2005, code zi, funded by aci jeunes chercheurs, université de montpellier ii, eopg strasbourg.* RESIF - Réseau Sismologique et géodésique Français. Retrieved from https://seismology.resif.fr/networks/#/ZI__2001 doi: 10.15778/RESIF.ZI2001

BAS, National Institute of Geophysics, Geodesy and Geography. (1980). *National seismic network of bulgaria.* International Federation of Digital Seismograph Networks. Retrieved from https://www.fdsn.org/networks/detail/BS/ doi: 10.7914/SN/BS

Bastow, I., Ogden, C., Pilidou, S., Dimitriados, I., Iosif, P., & Constantinou, C. (2016). *Troodos: Tomography and receiver function observations of an ophiolite using data obtained from seismology.* International Federation of Digital Seismograph Networks. Retrieved from https://www.fdsn.org/networks/detail/3K_2016/ doi: 10.7914/SN/3K_2016

Beyreuther, M., Barsch, R., Krischer, L., Megies, T., Behr, Y., & Wassermann, J. (2010). ObsPy: A Python Toolbox for Seismology. *Seismological Research Letters*, *81*(3), 530–533. Retrieved 2024-07-25, from https://doi.org/10.1785/gssrl.81.3.530 doi: 10.1785/gssrl.81.3.530

BGR. (1976). *German regional seismic network (grsn).* Bundesanstalt für Geowissenschaften und Rohstoffe. Retrieved from https://www.seismologie.bgr.de/doi/grsn/ doi: 10.25928/MBX6-HR74

Biryol, C. B., Beck, S. L., Zandt, G., & Özacar, A. A. (2011). Segmented african lithosphere beneath the anatolian region inferred from teleseismic p-wave tomography: Segmented lithosphere beneath anatolia. , *184*(3),

1037–1057. Retrieved 2026-07-31, from https://academic.oup.com/gji/article-lookup/doi/10.1111/j.1365-246X.2010.04910.x doi: 10.1111/j.1365-246X.2010.04910.x

Bozdağ, E., Desilva, S., Nolet, G., Orsvuran, R., Gok, R., Tarabulsi, Y. M., ... Mousa, A. (2025). P-Wave Arrival-Time Tomography of the Middle East Using ISC-EHB and Waveform Data. *Seismica*, *4*(1). Retrieved 2025-08-21, from https://seismica.library.mcgill.ca/article/view/1349 doi: 10.26443/seismica.v4i1.1349

Boğaziçi University, Kandilli Observatory And Earthquake Research Institute. (1971). *Kandilli observatory and earthquake research institute (koeri).* International Federation of Digital Seismograph Networks. Retrieved from https://www.fdsn.org/networks/detail/KO/ doi: 10.7914/SN/KO

Bunge, H. P., & Grand, S. P. (2000). Mesozoic plate-motion history below the northeast Pacific Ocean from seismic images of the subducted Farallon slab. *Nature 2000 405:6784*, *405*(6784), 337–340. Retrieved 2022-10-24, from https://www.nature.com/articles/35012586 doi: 10.1038/35012586

CAIAG, Central Asian Institute for Applied Geosciences. (2008). *Central asian seismic network of caiag.* International Federation of Digital Seismograph Networks. Retrieved from https://www.fdsn.org/networks/detail/KC/ doi: 10.7914/SN/KC

Calabria, U. D. (1981). *Rete sismica unical.* International Federation of Digital Seismograph Networks. Retrieved from https://www.fdsn.org/networks/detail/IY/ doi: 10.7914/SN/IY

Camp, V. E., & Roobol, M. J. (1992). Upwelling asthenosphere beneath western arabia and its regional implications. , *97*, 15255–15271. Retrieved 2026-07-16, from https://onlinelibrary.wiley.com/doi/abs/10.1029/92JB00943 (_eprint: https://agupubs.onlinelibrary.wiley.com/doi/pdf/10.1029/92JB00943) doi: 10.1029/92JB00943

CAREMON. (2009). *Caremon central asian cross-border network.* FDSN network code CK (2009–present); no DOI registered, see https://www.fdsn.org/networks/. International Federation of Digital Seismograph Networks.

Charles University in Prague, Institute of Geonics, Institute of Geophysics, Academy of Sciences of the Czech Republic, Institute of Physics of the Earth Masaryk University, & Institute of Rock Structure and Mechanics. (1973). *Czech regional seismic network.* International Federation of Digital Seismograph Networks. Retrieved from https://www.fdsn.org/networks/detail/CZ/ doi: 10.7914/SN/CZ

Chen, Y.-W., Wu, J., & Suppe, J. (2019). Southward propagation of Nazca subduction along the Andes. *Nature*, *565*(7740), 441–447. Retrieved 2024-06-28, from https://www.nature.com/articles/s41586-018-0860-1 doi: 10.1038/s41586-018-0860-1

Chevrot, S., Sylvander, M., & RESIF. (2017). *Seismic network x7:pyrope pyrenean observational portable experiment (resif-sismob).* RESIF - Réseau Sismologique et géodésique Français. Retrieved from https://seismology.resif.fr/networks/#/X7__2010 doi: 10.15778/RESIF.X72010

Chiarabba, C., Costanzo, A., De Gori, P., Del Gaudio, P., Falcone, S., Fonzetti, R., ... Pezzo, G. (2022). *Pollino broad-band near fault observatory (2022-2033), southern italy.* Istituto Nazionale di Geofisica e Vulcanologia (INGV). Retrieved from https://eida.ingv.it/en/network/XE_2022 doi: 10.13127/SD/NS6HB3Q8VE

Chiu, H.-Y., Chung, S.-L., Zarrinkoub, M. H., Mohammadi, S. S., Khatib, M. M., & Iizuka, Y. (2013). Zircon u–pb age constraints from iran on the magmatic evolution related to neotethyan subduction and zagros orogeny. , *162-163*, 70–87. Retrieved 2024-10-06, from https://www.sciencedirect.com/science/article/pii/S002449371300011X doi: 10.1016/j.lithos.2013.01.006

Clennett, E. J., Sigloch, K., Mihalynuk, M. G., Seton, M., Henderson, M. A., Hosseini, K., ... Müller, R. D. (2020). A Quantitative Tomotectonic Plate Reconstruction of Western North America and the Eastern Pacific Basin. *Geochemistry, Geophysics, Geosystems*, *21*(8), e2020GC009117. doi: 10.1029/2020gc009117

Corinth Rift Laboratory Team, & Epos-France. (2013). *Cl - corinth rift laboratory seismological network (crlnet).* RESIF - Réseau Sismologique et géodésique Français. Retrieved from `https://seismology.resif.fr/networks/#/CL` doi: 10.15778/RESIF.CL

Costanzo, A., Falcone, S., La Piana, C., Caserta, A., Doumaz, F., Buongiorno, M. F., ... Speciale, S. (2022). *Urban seismic network (rusn-cal-ingv) - real time urban seismic network managed by calabrian headquarters of ingv for monitoring urban areas, critical infrastructures and cultural heritage sites.* Istituto Nazionale di Geofisica e Vulcanologia (INGV). Retrieved from `https://eida.ingv.it/en/network/7C_2021` doi: 10.13127/SD/O5NRHMP9N7

DANA. (2012). *Dense array for north anatolia.* International Federation of Digital Seismograph Networks. Retrieved from `https://www.fdsn.org/networks/detail/YH_2012/` doi: 10.7914/SN/YH_2012

Darin, M. H., & Umhoefer, P. J. (2022). Diachronous initiation of Arabia–Eurasia collision from eastern Anatolia to the southeastern Zagros Mountains since middle Eocene time. *International Geology Review*, *64*(18), 2653–2681. Retrieved 2024-06-07, from `https://doi.org/10.1080/00206814.2022.2048272` doi: 10.1080/00206814.2022.2048272

Disaster and Emergency Management Authority. (1990). *Turkish national seismic network.* Department of Earthquake, Disaster and Emergency Management Authority. Retrieved from `https://www.fdsn.org/networks/detail/TU/` doi: 10.7914/SN/TU

Dziewonski, A. M., Chou, T.-A., & Woodhouse, J. H. (1981). Determination of earthquake source parameters from waveform data for studies of global and regional seismicity. *Journal of Geophysical Research: Solid Earth*, *86*(B4), 2825–2852. Retrieved 2024-06-05, from `https://onlinelibrary.wiley.com/doi/abs/10.1029/JB086iB04p02825` doi: 10.1029/JB086iB04p02825

EarthScope Consortium. (1986). *Global seismograph network - ii.* International Federation of Digital Seismograph Networks. Retrieved from `https://www.fdsn.org/networks/detail/II/` doi: 10.7914/SN/II

Ebinger, C. (2007). *Afar07.* International Federation of Digital Seismograph Networks. Retrieved from `https://www.fdsn.org/networks/detail/ZE_2007/` doi: 10.7914/SN/ZE_2007

Eibl, E., Walter, T., Jousset, P., Dahm, T., Allahbakhshi, M., Müller, D., & Hersir, G. P. (2020). *1 year seismological experiment at strokkur in 2017/18.* GFZ Data Services. Retrieved from `https://geofon.gfz.de/doi/network/7L/2017` doi: 10.14470/2Y7562610816

Ekström, G., Nettles, M., & Dziewoński, A. M. (2012). The global CMT project 2004–2010: Centroid-moment tensors for 13,017 earthquakes. *Physics of the Earth and Planetary Interiors*, *Complete*(200-201), 1–9. Retrieved 2024-06-05, from `https://www.infona.pl//resource/bwmeta1.element.elsevier-5bc59576-3fbd-357a-a5a3-11ad7ce73e0f` doi: 10.1016/j.pepi.2012.04.002

Endo, E., Zahran, H., Nofal, H., & Hadidy, S. (2007). The Saudi National Seismic Network. *Seismological Research Letters*, *78*(4), 439–445. Retrieved 2024-07-23, from `https://doi.org/10.1785/gssrl.78.4.439` doi: 10.1785/gssrl.78.4.439

ESI SAS, former GPI SAS (Geophysical Institute of the Slovak Academy of Sciences). (2004). *National network of seismic stations of slovakia.* GFZ Data Services. Retrieved from `http://geofon.gfz.de/doi/network/SK` doi: 10.14470/FX099882

Faccenna, C., Becker, T. W., Jolivet, L., & Keskin, M. (2013). Mantle convection in the middle east: Reconciling afar upwelling, arabia indentation and aegean trench rollback. , *375*, 254–269. Retrieved 2026-08-06, from https://www.sciencedirect.com/science/article/pii/S0012821X13002975 doi: 10.1016/j.epsl.2013.05.043

Fakhari, M. D., Axen, G. J., Horton, B. K., Hassanzadeh, J., & Amini, A. (2008). Revised age of proximal deposits in the zagros foreland basin and implications for cenozoic evolution of the high zagros. , *451*(1), 170–185. Retrieved 2024-08-08, from https://www.sciencedirect.com/science/article/pii/S0040195107004180 doi: 10.1016/j.tecto.2007.11.064

Fichtner, A., Bunge, H. P., & Igel, H. (2006). The adjoint method in seismology—: II. Applications: traveltimes and sensitivity functionals. *Physics of the Earth and Planetary Interiors*, *157*(1), 105–123. Retrieved 2024-06-05, from https://www.sciencedirect.com/science/article/pii/S0031920106001038 doi: 10.1016/j.pepi.2006.03.018

Fichtner, A., Kennett, B. L. N., Igel, H., & Bunge, H.-P. (2009). Full seismic waveform tomography for upper-mantle structure in the australasian region using adjoint methods. , *179*(3), 1703–1725. Retrieved 2026-08-06, from https://doi.org/10.1111/j.1365-246X.2009.04368.x doi: 10.1111/j.1365-246X.2009.04368.x

Fichtner, A., & van Leeuwen, T. (2015). Resolution analysis by random probing. *Journal of Geophysical Research: Solid Earth*, *120*(8), 5549–5573. Retrieved 2024-07-12, from https://onlinelibrary.wiley.com/doi/abs/10.1002/2015JB012106 doi: 10.1002/2015JB012106

Fletcher, R., & Reeves, C. M. (1964). Function minimization by conjugate gradients. *The Computer Journal*, *7*(2), 149–154. Retrieved 2024-06-05, from https://doi.org/10.1093/comjnl/7.2.149 doi: 10.1093/comjnl/7.2.149

Fontaine, F. R., Barruol, G., & Gonzalez, A. (2015). *Rivière des pluies project, la réunion island, 2015-2018.* RESIF - Réseau Sismologique et géodésique Français. Retrieved from https://seismology.resif.fr/networks/#/ZF_2015 doi: 10.15778/RESIF.ZF2015

Friederich, W., & Meier, T. (2005). *Egelados project 2005/07, rub bochum, germany.* GFZ Data Services. Retrieved from http://geofon.gfz.de/doi/network/Z3/2005 doi: 10.14470/M87550267382

Fuston, S., & Wu, J. (2020). Raising the Resurrection plate from an unfolded-slab plate tectonic reconstruction of northwestern North America since early Cenozoic time. *GSA Bulletin*, *133*(5-6), 1128–1140. Retrieved 2024-04-12, from https://doi.org/10.1130/B35677.1 doi: 10.1130/B35677.1

Gao, S. (2009). *Afar depression dense seismic array.* International Federation of Digital Seismograph Networks. Retrieved from https://www.fdsn.org/networks/detail/ZK_2009/ doi: 10.7914/SN/ZK_2009

GEOFON. (2000). *Desert.* FDSN network code ZR (2000–2004); no DOI registered, see https://www.fdsn.org/networks/. International Federation of Digital Seismograph Networks.

GEOFON Data Centre. (1993). *Geofon seismic network.* GFZ Data Services. Retrieved from http://geofon.gfz.de/doi/network/GE doi: 10.14470/TR560404

Geological and Seismological Institute of Moldova. (2007). *Moldova digital seismic network.* International Federation of Digital Seismograph Networks. Retrieved from https://www.fdsn.org/networks/detail/MD/ doi: 10.7914/SN/MD

Geological Survey Department Cyprus. (2013). *Cyprus broadband seismological network.* International Federation of Digital Seismograph Networks. Retrieved from https://www.fdsn.org/networks/detail/CQ/ doi: 10.7914/SN/CQ

Geosciences Barcelona, & Institute Earth Sciences "Jaume Almera". (2007). *Iberarray.* International Federation of Digital Seismograph Networks. Retrieved from

https://www.fdsn.org/networks/detail/IB/ doi: 10.7914/SN/IB

Gernon, T. M., Hincks, T. K., Brune, S., Braun, J., Jones, S. M., Keir, D., ... Glerum, A. (2024). Coevolution of craton margins and interiors during continental break-up. *Nature*, *632*(8024), 327–335. Retrieved 2024-10-19, from https://www.nature.com/articles/s41586-024-07717-1 doi: 10.1038/s41586-024-07717-1

Gernon, T. M., Jones, S. M., Brune, S., Hincks, T. K., Palmer, M. R., Schumacher, J. C., ... Glerum, A. (2023). Rift-induced disruption of cratonic keels drives kimberlite volcanism. *Nature*, *620*(7973), 344–350. Retrieved 2024-05-22, from https://www.nature.com/articles/s41586-023-06193-3 doi: 10.1038/s41586-023-06193-3

Guest, B., Stockli, D. F., Grove, M., Axen, G. J., Lam, P. S., & Hassanzadeh, J. (2006). Thermal histories from the central Alborz Mountains, northern Iran: Implications for the spatial and temporal distribution of deformation in northern Iran. *Bulletin of the Geological Society of America*, *118*(11-12), 1507–1521. doi: 10.1130/B25819.1

Göğüş, O. H., Pysklywec, R. N., Şengör, A. M. C., & Gün, E. (2017). Drip tectonics and the enigmatic uplift of the Central Anatolian Plateau. *Nature Communications*, *8*(1), 1538. Retrieved 2026-09-14, from https://www.nature.com/articles/s41467-017-01611-3 doi: 10.1038/s41467-017-01611-3

Gürer, D., & van Hinsbergen, D. J. (2019). Diachronous demise of the neotethys ocean as a driver for non-cylindrical orogenesis in anatolia. , *760*, 95–106. doi: 10.1016/j.tecto.2018.06.005

Haberland, C., Wetzel, H.-U., Schurr, B., Abdybachaev, U., Orunbaev, S., & Sharshebaev, A. (2009). *Ferghana project.* GFZ Data Services. Retrieved from https://geofon.gfz.de/doi/network/6C/2009 doi: 10.14470/1P035555

Hafkenscheid, E., Wortel, M. J., & Spakman, W. (2006). Subduction history of the Tethyan region derived from seismic tomography and tectonic reconstructions. *Journal of Geophysical Research: Solid Earth*, *111*(B8), 8401. Retrieved 2023-02-06, from https://onlinelibrary.wiley.com/doi/full/10.1029/2005JB003791 doi: 10.1029/2005JB003791

Hammond, J., Goitom, B., Kendall, J. M., & Ogubazghi, G. (2011a). *Eritrea seismic project.* International Federation of Digital Seismograph Networks. Retrieved from https://www.fdsn.org/networks/detail/5H_2011/ doi: 10.7914/SN/5H_2011

Hammond, J., Goitom, B., Kendall, J. M., & Ogubazghi, G. (2011b). *Nabro urgency array.* International Federation of Digital Seismograph Networks. Retrieved from https://www.fdsn.org/networks/detail/4H_2011/ doi: 10.7914/SN/4H_2011

Harjes, H.-P. (1996). *Temporary networks 1996-2002 on crete, rub bochum, germany.* GFZ Data Services. Retrieved from http://geofon.gfz.de/doi/network/YU/1996 doi: 10.14470/LH6441260253

Harzhauser, M., Kroh, A., Mandic, O., Piller, W. E., Göhlich, U., Reuter, M., & Berning, B. (2007). Biogeographic responses to geodynamics: A key study all around the oligo–miocene tethyan seaway. , *246*(4), 241–256. Retrieved 2024-10-06, from https://www.sciencedirect.com/science/article/pii/S0044523107000186 doi: 10.1016/j.jcz.2007.05.001

Heilman, E., & Becker, T. W. (2022). Plume-slab interactions can shut off subduction. , *49*(13), e2022GL099286. Retrieved 2026-07-31, from https://agupubs.onlinelibrary.wiley.com/doi/10.1029/2022GL099286 doi: 10.1029/2022GL099286

Helffrich, G. (2006). *Syros (cyclades).* International Federation of Digital Seismograph Networks. Retrieved from https://www.fdsn.org/networks/detail/6C_2006/ doi: 10.7914/QPTA-1D71

Hestenes, M. R., & Steifel, E. (1952). Methods of conjugate gradients for solving lin-

ear systems. *Journal of Research of the National Bureau of Standards*, *49*(6), 409–436.

Hua, J., Grand, S. P., Becker, T. W., Janiszewski, H. A., Liu, C., Trugman, D. T., & Zhu, H. (2025). Seismic full-waveform tomography of active cratonic thinning beneath North America consistent with slab-induced dripping. *Nature Geoscience*, *18*(4), 358–364. Retrieved 2026-07-10, from https://www.nature.com/articles/s41561-025-01671-x doi: 10.1038/s41561-025-01671-x

IGPCEA. (2000). *China national seismic network, data management centre of china national seismic network at institute of geophysics, cea.* International Federation of Digital Seismograph Networks. Retrieved from https://www.fdsn.org/networks/detail/CB/ doi: 10.7914/SN/CB

IHMS, Sector for Seismology, Institute of Hydrometeorology and Seismology of Montenegro. (1982). *Montenegrin seismic network.* International Federation of Digital Seismograph Networks. Retrieved from https://www.fdsn.org/networks/detail/ME/ doi: 10.7914/SN/ME

Ilia State University, Seismic Monitoring Centre of Georgia. (1988). *National seismic network of georgia.* International Federation of Digital Seismograph Networks. Retrieved from https://www.fdsn.org/networks/detail/GO/ doi: 10.7914/1YX9-8844

Inati, L., Zeyen, H., Nader, F. H., Adelinet, M., Sursock, A., Rahhal, M. E., & Roure, F. (2016). Lithospheric architecture of the Levant Basin (Eastern Mediterranean region): A 2D modeling approach. *Tectonophysics*, *693*, 143–156. Retrieved 2024-06-27, from https://www.sciencedirect.com/science/article/pii/S0040195116304838 doi: 10.1016/j.tecto.2016.10.030

INGV. (2005). *Rete sismica nazionale (rsn).* Istituto Nazionale di Geofisica e Vulcanologia (INGV). Retrieved from https://eida.ingv.it/en/network/IV doi: 10.13127/SD/X0FXNH7QFY

INGV. (2008). *Ingv experiments network.* FDSN network code TV (2008–present); no DOI registered, see https://www.fdsn.org/networks/. International Federation of Digital Seismograph Networks.

INGV. (2020). *Temporary network seismic in central calabria.* FDSN network code XK (2020–2020); no DOI registered, see https://www.fdsn.org/networks/. International Federation of Digital Seismograph Networks.

IPGP. (2008). *Gnss, seismic broadband and strong motion permanent networks in west indies.* Institut de physique du globe de Paris (IPGP), Université de Paris. Retrieved from http://volobsis.ipgp.fr/networks/detail/WI/ doi: 10.18715/ANTILLES.WI

IPGP, & EOST. (1982). *Geoscope, french global network of broad band seismic stations.* Institut de physique du globe de Paris, Université Paris Cité. Retrieved from http://geoscope.ipgp.fr/networks/detail/G/ doi: 10.18715/GEOSCOPE.G

Israel seismic network. (1982). FDSN network code IS (1982–present); no DOI registered, see https://www.fdsn.org/networks/. International Federation of Digital Seismograph Networks.

ISTerre. (2005). *Dhofar seismic experiment ii.* FDSN network code YR (2005–2007); no DOI registered, see https://www.fdsn.org/networks/. International Federation of Digital Seismograph Networks.

Joffe, S., & Garfunkel, Z. (1987). Plate kinematics of the circum Red Sea—a re-evaluation. *Tectonophysics*, *141*(1), 5–22. Retrieved 2024-10-14, from https://www.sciencedirect.com/science/article/pii/0040195187901715 doi: 10.1016/0040-1951(87)90171-5

Jolivet, L., & Faccenna, C. (2000). Mediterranean extension and the Africa-Eurasia collision. *Tectonics*, *19*(6), 1095–1106. Retrieved 2021-05-05, from https://agupubs.onlinelibrary.wiley.com/doi/full/10.1029/2000TC900018 doi:

10.1029/2000TC900018

Kaviani, A., Sandvol, E., Moradi, A., Rümpker, G., Tang, Z., & Mai, P. M. (2018). Mantle Transition Zone Thickness Beneath the Middle East: Evidence for Segmented Tethyan Slabs, Delaminated Lithosphere, and Lower Mantle Upwelling. *Journal of Geophysical Research: Solid Earth*, *123*(6), 4886–4905. Retrieved 2024-01-18, from https://onlinelibrary.wiley.com/doi/abs/10.1029/2018JB015627 doi: 10.1029/2018JB015627

Keir, D., Doubre, C., & Leroy, S. (2017). *Afar margin northern profile.* International Federation of Digital Seismograph Networks. Retrieved from https://www.fdsn.org/networks/detail/YQ_2017/ doi: 10.7914/SN/YQ_2017

Keir, D., & Hammond, J. O. (2009). *Afar0911.* International Federation of Digital Seismograph Networks. Retrieved from https://www.fdsn.org/networks/detail/2H_2009/ doi: 10.7914/SN/2H_2009

Kennett, B. L. N., Engdahl, E. R., & Buland, R. (1995). Constraints on seismic velocities in the Earth from traveltimes. *Geophysical Journal International*, *122*(1), 108–124. Retrieved 2024-04-04, from https://doi.org/10.1111/j.1365-246X.1995.tb03540.x doi: 10.1111/j.1365-246X.1995.tb03540.x

Keranen, K. (2013). *Exploring extensional tectonics beyond the ethiopian rift.* International Federation of Digital Seismograph Networks. Retrieved from https://www.fdsn.org/networks/detail/YY_2013/ doi: 10.7914/SN/YY_2013

KIS, & UC San Diego. (1991). *Kyrgyz seismic telemetry network.* International Federation of Digital Seismograph Networks. Retrieved from https://www.fdsn.org/networks/detail/KN/ doi: 10.7914/SN/KN

KIS, Kyrgyz Institute of Seismology. (2007). *Kyrgyz digital network.* International Federation of Digital Seismograph Networks. Retrieved from https://www.fdsn.org/networks/detail/KR/ doi: 10.7914/SN/KR

KNDC. (1994). *Kazakhstan network.* International Federation of Digital Seismograph Networks. Retrieved from https://www.fdsn.org/networks/detail/KZ/ doi: 10.7914/SN/KZ

Komatitsch, D., & Tromp, J. (2002a). Spectral-element simulations of global seismic wave propagation-I. Validation. *Geophysical Journal International*, *149*(2), 390–412. Retrieved 2024-06-05, from https://academic.oup.com/gji/article/149/2/390/727101 doi: 10.1046/j.1365-246X.2002.01653.x

Komatitsch, D., & Tromp, J. (2002b). Spectral-element simulations of global seismic wave propagation—II. Three-dimensional models, oceans, rotation and self-gravitation. *Geophysical Journal International*, *150*(1), 303–318. Retrieved 2024-06-05, from https://doi.org/10.1046/j.1365-246X.2002.01716.x doi: 10.1046/j.1365-246X.2002.01716.x

Kounoudis, R., Bastow, I. D., Ogden, C. S., Goes, S., Jenkins, J., Grant, B., & Braham, C. (2020). Seismic Tomographic Imaging of the Eastern Mediterranean Mantle: Implications for Terminal-Stage Subduction, the Uplift of Anatolia, and the Development of the North Anatolian Fault. *Geochemistry, Geophysics, Geosystems*, *21*(7), e2020GC009009. Retrieved 2024-06-06, from https://onlinelibrary.wiley.com/doi/abs/10.1029/2020GC009009 doi: 10.1029/2020GC009009

Kuwait national seismic network. (1997). FDSN network code KW (1997–present); no DOI registered, see https://www.fdsn.org/networks/. International Federation of Digital Seismograph Networks.

Kövesligethy Radó Seismological Observatory, Geodetic And Geophysical Institute, Research Centre For Astronomy And Earth Sciences, Hungarian Academy Of Sciences (MTA CSFK GGI KRSZO). (1992). *Hungarian national seismological network.* GFZ Data Services. Retrieved from https://geofon.gfz.de/doi/network/HU doi: 10.14470/UH028726

Laske, G., Masters, G., Ma, Z., & Pasyanos, M. (2013). Update on CRUST1. 0—A 1-degree global model of Earth's crust. In *Geophysical Research Abstracts* (p. 2658). Vienna, Austria.

Leroy, S. (2003). *Dhofar seismic experiment.* International Federation of Digital Seismograph Networks. Retrieved from https://www.fdsn.org/networks/detail/XZ_2003/ doi: 10.7914/SN/XZ_2003

Leroy, S., Keir, D., & Stuart, G. (2009). *Young conjugate margins lab in the gulf of aden.* International Federation of Digital Seismograph Networks. Retrieved from https://www.fdsn.org/networks/detail/XW_2009/ doi: 10.7914/SN/XW_2009

Levèque, J.-J., & RESIF. (2010). *Horn of africa (ethiopa, yemen) broad-band experiment (horn of africa, resif-sismob).* RESIF - Réseau Sismologique et géodésique Français. Retrieved from https://seismology.resif.fr/networks/#/YR__1999 doi: 10.15778/RESIF.YR1999

Li, Z.-H., Liu, M., & Gerya, T. (2016). Lithosphere delamination in continental collisional orogens: A systematic numerical study. *Journal of Geophysical Research: Solid Earth*, *121*(7), 5186–5211. Retrieved 2024-10-17, from https://onlinelibrary.wiley.com/doi/abs/10.1002/2016JB013106 doi: 10.1002/2016JB013106

Liu, C., Banerjee, R., Grand, S. P., Sandvol, E., Mitra, S., Liang, X., & Wei, S. (2024). A high-resolution seismic velocity model for East Asia using full-waveform tomography: Constraints on India-Asia collisional tectonics. *Earth and Planetary Science Letters*, *639*, 118764. Retrieved 2024-07-08, from https://www.sciencedirect.com/science/article/pii/S0012821X24001973 doi: 10.1016/j.epsl.2024.118764

Mackey, K. (2021). *Mangystau array (msuar) feasibility study.* International Federation of Digital Seismograph Networks. Retrieved from https://www.fdsn.org/networks/detail/YL_2021/ doi: 10.7914/SN/YL_2021

Malet, J.-P., Hibert, C., Radiguet, M., Gautier, S., Larose, E., Amitrano, D., ... RESIF (2015). *French landslide observatory – omiv (temporary data) (mt-campagne) (resif - sismob).* RESIF - Réseau Sismologique et géodésique Français. Retrieved from https://seismology.resif.fr/networks/#/1N__2015 doi: 10.15778/RESIF.1N2015

McGuire, A. V. (1988). The mantle beneath the Red Sea margin: xenoliths from western Saudi Arabia. *Tectonophysics*, *150*(1), 101–119. Retrieved 2024-10-14, from https://www.sciencedirect.com/science/article/pii/0040195188902971 doi: 10.1016/0040-1951(88)90297-1

McQuarrie, N., & van Hinsbergen, D. J. (2013). Retrodeforming the Arabia-Eurasia collision zone: Age of collision versus magnitude of continental subduction. *Geology*, *41*(3), 315–318. Retrieved 2021-05-05, from www.gsapubs.org doi: 10.1130/G33591.1

MedNet. (1990). *Mediterranean very broadband seismographic network (mednet).* Istituto Nazionale di Geofisica e Vulcanologia (INGV). Retrieved from https://eida.ingv.it/en/network/MN doi: 10.13127/SD/FBBBTDTD6Q

Meier, T., Bohnhoff, M., & Harjes, H.-P. (2004). *Cyclades project 2002-2005 and libyan sea offshore project 2003-2004, rub bochum, germany.* GFZ Data Services. Retrieved from http://geofon.gfz.de/doi/network/ZZ/2002 doi: 10.14470/MM7557265463

Metaxian, J.-P., Surono, Widiyantoro, S., & RESIF. (2018). *Seismic network yr:domerapi temporary experiment (resif-sismob.* RESIF - Réseau Sismologique et géodésique Français. Retrieved from https://seismology.resif.fr/networks/#/YR__2013 doi: 10.15778/RESIF.YR2013

Moretti, M., Margheriti, L., Alparone, S., Costanzo, A., La Rocca, M., Murphy, S., ... Focus Working Group (2021). *Seismic data acquired by focusx temporary land-network (fxland), southern italy.* Istituto Nazionale di Geofisica e

Vulcanologia (INGV). Retrieved from https://eida.ingv.it/en/network/1J_2021 doi: 10.13127/SD/O5QWM6WJCD

Multiple Operators. (1997). *International geodynamics and earth tide service.* International Federation of Digital Seismograph Networks. Retrieved from https://www.fdsn.org/networks/detail/SG/ doi: 10.7914/SN/SG

Müller, R. D., Zahirovic, S., Williams, S. E., Cannon, J., Seton, M., Bower, D. J., ... Gurnis, M. (2019). A Global Plate Model Including Lithospheric Deformation Along Major Rifts and Orogens Since the Triassic. *Tectonics*, *38*(6), 1884–1907. doi: 10.1029/2018TC005462

NAS RA, Institute Of Geological Sciences. (2022). *Armenian seismological network.* International Federation of Digital Seismograph Networks. Retrieved from https://www.fdsn.org/networks/detail/A2/ doi: 10.7914/SN/A2

National Academy of sciences of Tajikistan. (2009). *Tajikistan national seismic network.* International Federation of Digital Seismograph Networks. Retrieved from https://www.fdsn.org/networks/detail/TJ/ doi: 10.7914/SN/TJ

National Institute for Earth Physics. (1994). *Romanian seismic network.* International Federation of Digital Seismograph Networks. Retrieved from https://www.fdsn.org/networks/detail/RO/ doi: 10.7914/SN/RO

National Observatory of Athens, Institute of Geodynamics, Athens. (1975). *Hellenic unified seismological network.* International Federation of Digital Seismograph Networks. Retrieved from https://www.fdsn.org/networks/detail/HL/ doi: 10.7914/SN/HL

Nisyros network. (2007). FDSN network code 6E (2007–2011); no DOI registered, see https://www.fdsn.org/networks/. International Federation of Digital Seismograph Networks.

Obermann, A., Jozinović, D., Cvijic, S., Krehić, A., & Swiss Seismological Service (SED) at ETH Zurich. (2022). *Swiss contribution to adriaarray temporary network.* ETH Zurich. Retrieved from https://networks.seismo.ethz.ch/en/networks/y5 doi: 10.12686/SED/NETWORKS/Y5

OIMV. (2006). *Observatoire multi-disciplinaire des instabilités de versants (omiv).* RESIF - Réseau Sismologique et géodésique Français. Retrieved from https://seismology.resif.fr/networks/#/MT doi: 10.15778/RESIF.MT

OVPF, & IPGP. (2008). *Seismic, tiltmeter, extensometer, magnetic and weather permanent networks on piton de la fournaise volcano and la réunion.* Institut de physique du globe de Paris (IPGP), Université de Paris. Retrieved from http://volobsis.ipgp.fr/networks/detail/PF doi: 10.18715/REUNION.PF

Passarelli, L., Govoni, A., Maccaferri, F., Woith, H., Strollo, A., Zieke, T., ... Dahm, T. (2017). *East pollino experiment, southern italy.* GFZ Data Services. Retrieved from http://geofon.gfz.de/doi/network/YZ/2017 doi: 10.14470/LM582526

Paul, A., Hatzfeld, D., Mokhtari, M., & RESIF. (2000). *Seismic network yb:central zagros lithospheric transect (resif-sismob).* RESIF - Réseau Sismologique et géodésique Français. Retrieved from https://seismology.resif.fr/networks/#/YB__2000 doi: 10.15778/RESIF.YB2000

Paul, A., Hatzfeld, D., Tatar, M., & Mokhtari, M. (2006). *Seismic network zh:north zagros lithospheric transect (resif-sismob).* RESIF - Réseau Sismologique et géodésique Français. Retrieved from https://seismology.resif.fr/networks/#/ZH__2003 doi: 10.15778/RESIF.ZH2003

Paul, A., Karabulut, H., & RESIF. (2007). *Seismic network xw:simbaad temporary experiment - anatolia western transect (resif-sismob).* RESIF - Réseau Sismologique et géodésique Français. Retrieved from https://seismology.resif.fr/networks/#/XW__2007 doi: 10.15778/RESIF.XW2007

Paul, A., Karabulut, H., & RESIF. (2008). *Seismic network yi:simbaad temporary experiment - anatolia eastern transect (resif-sismob).* RESIF - Réseau Sis-

mologique et géodésique Français. Retrieved from https://seismology.resif.fr/networks/#/YI_2008 doi: 10.15778/RESIF.YI2008

Paul, A., Karabulut, H., & RESIF. (2013). *Seismic network xy:simbaad temporary experiment - backbone of broadband stations.* RESIF - Réseau Sismologique et géodésique Français. Retrieved from https://seismology.resif.fr/networks/#/XY_2007 doi: 10.15778/RESIF.XY2007

Pelletier, B., Lyon-Caen, H., RESIF, & Parc national sismologique mobile (SisMob). (2018). *Post-sismic experiment after 8th june 2008 movri (greece) event (peloponesus).* RESIF - Réseau Sismologique et géodésique Français. Retrieved from https://seismology.resif.fr/networks/#/1E_2008 doi: 10.15778/RESIF.1E2008

Penn State University. (2004). *Africaarray.* International Federation of Digital Seismograph Networks. Retrieved from https://www.fdsn.org/networks/detail/AF/ doi: 10.7914/SN/AF

Polish Academy of Sciences, t. . P. p. . I. y. . ., Institute of Geophysics. (n.d.). Retrieved from https://www.fdsn.org/networks/detail/PL/ doi: 10.7914/90RH-0Q80

Polytechnic University of Tirana, Institute of Geosciences. (2002). *Albanian seismological network.* International Federation of Digital Seismograph Networks. Retrieved from https://www.fdsn.org/networks/detail/AC/ doi: 10.7914/SN/AC

Portner, D. E., Beck, S., Zandt, G., & Scire, A. (2017). The nature of subslab slow velocity anomalies beneath south america. , *44*(10), 4747–4755. Retrieved 2026-07-31, from https://agupubs.onlinelibrary.wiley.com/doi/10.1002/2017GL073106 doi: 10.1002/2017GL073106

Portner, D. E., Delph, J. R., Biryol, C. B., Beck, S. L., Zandt, G., Özacar, A. A., ... Türkelli, N. (2018). Subduction termination through progressive slab deformation across Eastern Mediterranean subduction zones from updated P-wave tomography beneath Anatolia. *Geosphere*, *14*(3), 907–925. Retrieved 2026-09-14, from https://doi.org/10.1130/GES01617.1 doi: 10.1130/GES01617.1

Province südtirol. (2006). FDSN network code SI (2006–present); no DOI registered, see https://www.fdsn.org/networks/. International Federation of Digital Seismograph Networks.

Ricard, Y., Richards, M., Lithgow-Bertelloni, C., & Le Stunff, Y. (1993). A geodynamic model of mantle density heterogeneity. , *98*, 21895–21909. Retrieved from https://onlinelibrary.wiley.com/doi/full/10.1029/93JB02216 doi: 10.1029/93JB02216

Ritsema, J., Deuss, A., van Heijst, H. J., & Woodhouse, J. H. (2011). S40RTS: a degree-40 shear-velocity model for the mantle from new Rayleigh wave dispersion, teleseismic traveltime and normal-mode splitting function measurements. *Geophysical Journal International*, *184*(3), 1223–1236. Retrieved 2024-02-28, from https://doi.org/10.1111/j.1365-246X.2010.04884.x doi: 10.1111/j.1365-246X.2010.04884.x

Ritsema, J., & van Heijst, H.-J. (2002). Constraints on the correlation of P- and S-wave velocity heterogeneity in the mantle from P, PP, PPP and PKPab traveltimes. *Geophysical Journal International*, *149*(2), 482–489. Retrieved 2024-02-28, from https://doi.org/10.1046/j.1365-246X.2002.01631.x doi: 10.1046/j.1365-246X.2002.01631.x

Rodgers, A. J., Krischer, L., Afanasiev, M., Boehm, C., Doody, C., & Simmons, N. (2024). Adjoint Waveform Tomography for Crustal and Upper Mantle Structure of the Middle East and Southwest Asia for Improved Waveform Simulations Using Openly Available Broadband Data. *Bulletin of the Seismological Society of America*, *114*(3), 1365–1391. Retrieved 2024-07-11, from https://doi.org/10.1785/0120230248 doi: 10.1785/0120230248

Roecker, S., & Levin, V. (2007). *Collaborative research: Imaging the upper mantle beneath the western tibetan plateau.* International Federation of Digital Seismograph Networks. Retrieved from https://www.fdsn.org/networks/detail/Y2_2007/ doi: 10.7914/SN/Y2_2007

Royal Holloway, University of London. (2005). *Boina broadband network.* FDSN network code YZ (2005–2007); no DOI registered, see https://www.fdsn.org/networks/. International Federation of Digital Seismograph Networks.

Rögl, F. (1999). Mediterranean and paratethys. facts and hypotheses of an oligocene to miocene paleogeography (short overview). , *50*(4), 339–349.

Sandvol, E. (2013). *Continental dynamics/central anatolian tectonics: Surface to mantle dynamics during collision to escape.* International Federation of Digital Seismograph Networks. Retrieved from https://www.fdsn.org/networks/detail/YB_2013/ doi: 10.7914/SN/YB_2013

Sandvol, E., Nabelek, J., & Mackey, K. (2017). *The caucasus seismic network: The uplift and structure of the greater and lesser caucasus.* International Federation of Digital Seismograph Networks. Retrieved from https://www.fdsn.org/networks/detail/XA_2017/ doi: 10.7914/SN/XA_2017

Schaeffer, A. J., & Lebedev, S. (2013). Global shear speed structure of the upper mantle and transition zone. *Geophysical Journal International*, *194*(1), 417–449. Retrieved 2024-10-14, from https://doi.org/10.1093/gji/ggt095 doi: 10.1093/gji/ggt095

Schurr, B., Yuan, X., Haberland, C., Mechie, J., & Kufner, S.-K. (2012). *Tiptimon (tien shan-pamir monitoring program) tajikistan (2012/2014).* GFZ Data Services. Retrieved from http://geofon.gfz.de/doi/network/5C/2012 doi: 10.14470/0P7567352807

Schurr, B., Yuan, X., Kufner, S., & Bloch, W. (2017). *Sarez pamir aftershock seismic network.* GFZ Data Services. Retrieved from http://geofon.gfz.de/doi/network/9H/2016 doi: 10.14470/4U7561589984

SEME, LTD Seismological Experience and Methodology Expedition of the Committee of Science of the Ministry of Education and Science of the Republic of Kazakhstan. (2003). *Seismic network of the seismological experience and methodology expedition cs mes rk.* International Federation of Digital Seismograph Networks. Retrieved from https://www.fdsn.org/networks/detail/QZ/ doi: 10.7914/SN/QZ

Seton, M., Müller, R. D., Zahirovic, S., Gaina, C., Torsvik, T., Shephard, G., ... Chandler, M. (2012). Global continental and ocean basin reconstructions since 200Ma. *Earth-Science Reviews*, *113*(3-4), 212–270. Retrieved from http://dx.doi.org/10.1016/j.earscirev.2012.03.002 doi: 10.1016/j.earscirev.2012.03.002

Sigloch, K., & Mihalynuk, M. G. (2013). Intra-oceanic subduction shaped the assembly of Cordilleran North America. *Nature*, *496*(7443), 50–56. Retrieved 2024-04-12, from https://www.nature.com/articles/nature12019 doi: 10.1038/nature12019

Sigloch, K., & Mihalynuk, M. G. (2017). Mantle and geological evidence for a Late Jurassic–Cretaceous suture spanning North America. *GSA Bulletin*, *129*(11-12), 1489–1520. Retrieved 2024-04-12, from https://doi.org/10.1130/B31529.1 doi: 10.1130/B31529.1

SLUB, & LSDAUoB. (2014). *Iraqi seismic observatory.* International Federation of Digital Seismograph Networks. Retrieved from https://www.fdsn.org/networks/detail/MP/ doi: 10.7914/SN/MP

Sobiesiak, M., & Schurr, B. (2007). *Taskforce tocopilla 2007.* GFZ Data Services. Retrieved from https://geofon.gfz.de/doi/network/Y9/2007 doi: 10.14470/L47552843299

Steinberger, B., Torsvik, T. H., & Becker, T. W. (2012). Subduction to the lower mantle – a comparison between geodynamic and tomographic mod-

els. *Solid Earth*, *3*(2), 415–432. Retrieved 2024-10-14, from https://se.copernicus.org/articles/3/415/2012/ doi: 10.5194/se-3-415-2012

Stern, R. J., & Johnson, P. (2010). Continental lithosphere of the Arabian Plate: A geologic, petrologic, and geophysical synthesis. *Earth-Science Reviews*, *101*(1), 29–67. Retrieved 2024-10-14, from https://www.sciencedirect.com/science/article/pii/S0012825210000152 doi: 10.1016/j.earscirev.2010.01.002

Tao, K., Grand, S. P., & Niu, F. (2017). Full-waveform inversion of triplicated data using a normalized-correlation-coefficient-based misfit function. *Geophysical Journal International*, *210*(3), 1517–1524. doi: 10.1093/gji/ggx249

Tao, K., Grand, S. P., & Niu, F. (2018). Seismic Structure of the Upper Mantle Beneath Eastern Asia From Full Waveform Seismic Tomography. *Geochemistry, Geophysics, Geosystems*, *19*, 2732–2763. Retrieved 2021-03-12, from https://doi.org/ doi: 10.1029/2018GC007460

Tarantola, A. (1984). Inversion of seismic reflection data in the acoustic approximation. *GEOPHYSICS*, *49*(8), 1259–1266. Retrieved 2024-06-05, from https://library.seg.org/doi/abs/10.1190/1.1441754 doi: 10.1190/1.1441754

Task force kirgistan. (2008). FDSN network code 4B (2008–2009); no DOI registered, see https://www.fdsn.org/networks/. International Federation of Digital Seismograph Networks.

Technological Educational Institute of Crete. (2006). *Seismological network of crete.* International Federation of Digital Seismograph Networks. Retrieved from https://www.fdsn.org/networks/detail/HC/ doi: 10.7914/SN/HC

Tetley, M. G., Williams, S. E., Gurnis, M., Flament, N., & Müller, R. D. (2019). Constraining Absolute Plate Motions Since the Triassic. *Journal of Geophysical Research: Solid Earth*, *124*(7), 7231–7258. Retrieved 2020-11-28, from https://onlinelibrary.wiley.com/doi/abs/10.1029/2019JB017442 doi: 10.1029/2019JB017442

Thrastarson, S., van Herwaarden, D., Noe, S., Josef Schiller, C., & Fichtner, A. (2024). REVEAL: A Global Full-Waveform Inversion Model. *Bulletin of the Seismological Society of America*, *114*(3), 1392–1406. Retrieved 2024-10-10, from https://doi.org/10.1785/0120230273 doi: 10.1785/0120230273

Tromp, J., Tape, C., & Liu, Q. (2005). Seismic tomography, adjoint methods, time reversal and banana-doughnut kernels. *Geophysical Journal International*, *160*(1), 195–216. doi: 10.1111/j.1365-246X.2004.02453.x

Unibas. (2005). FDSN network code BA (2005–present); no DOI registered, see https://www.fdsn.org/networks/. International Federation of Digital Seismograph Networks.

University of Athens. (2008). *Hellenic unified seismological network, university of athens, seismological laboratory.* International Federation of Digital Seismograph Networks. Retrieved from https://www.fdsn.org/networks/detail/HA/ doi: 10.7914/SN/HA

University of Bari "Aldo Moro". (2013). *Otrions.* International Federation of Digital Seismograph Networks. Retrieved from https://www.fdsn.org/networks/detail/OT/ doi: 10.7914/SN/OT

University of Bristol. (2007). *Afar consortium network.* FDSN network code ZF (2007–2009); no DOI registered, see https://www.fdsn.org/networks/. International Federation of Digital Seismograph Networks.

University of Leeds. (2005). *Carpathian basins project regional array.* FDSN network code YG (2005–2007); no DOI registered, see https://www.fdsn.org/networks/. International Federation of Digital Seismograph Networks.

University of Leeds. (2009). *South carpathian project.* FDSN network code YD (2009–2011); no DOI registered, see https://www.fdsn.org/networks/. International Federation of Digital Seismograph Networks.

University of Patras. (2000). *Hellenic unified seismological network.* International Federation of Digital Seismograph Networks. Retrieved from https://www.fdsn.org/networks/detail/HP/ doi: 10.7914/SN/HP

University of Zagreb. (2001). *Croatian seismograph network.* International Federation of Digital Seismograph Networks. Retrieved from https://www.fdsn.org/networks/detail/CR/ doi: 10.7914/SN/CR

University of Munchen, Department of Earth and Environmental Sciences, Geophysical Observatory. (2001). *Bayernnetz.* International Federation of Digital Seismograph Networks. Retrieved from https://www.fdsn.org/networks/detail/BW/ doi: 10.7914/SN/BW

van der Lee, S., Deschamps, A., Margheriti, L., & Giardini, D. (1999). *Midsea - mantle investigation of the deep suture between eurasia and africa.* International Federation of Digital Seismograph Networks. Retrieved from https://www.fdsn.org/networks/detail/YF_1999/ doi: 10.7914/SN/YF_1999

van der Meer, D. G., Spakman, W., Van Hinsbergen, D. J., Amaru, M. L., & Torsvik, T. H. (2010). Towards absolute plate motions constrained by lower-mantle slab remnants. *Nature Geoscience*, *3*(1), 36–40. Retrieved from http://dx.doi.org/10.1038/ngeo708 doi: 10.1038/ngeo708

Various Institutions. (1965). *International miscellaneous stations.* International Federation of Digital Seismograph Networks. Retrieved from https://www.fdsn.org/networks/detail/IM/ doi: 10.7914/VEFQ-VH75

Veisi, M., Sobouti, F., Chevrot, S., Abbasi, M., & Shabanian, E. (2021). Upper mantle structure under the Zagros collision zone; insights from 3D teleseismic P-wave tomography. *Tectonophysics*, *819*, 229106. Retrieved 2024-06-28, from https://www.sciencedirect.com/science/article/pii/S0040195121003887 doi: 10.1016/j.tecto.2021.229106

Vergne, J., Doubre, C., & Leroy, S. (2014). *Seismic network 7c:dora experiment (resif-sismob).* RESIF - Réseau Sismologique et géodésique Français. Retrieved from https://seismology.resif.fr/networks/#/7C__2009 doi: 10.15778/RESIF.7C2009

Weidle, C., Agard, P., Meier, T., Ducassou, C., & El-Hussain, I. (2013). *Cool (crust of the oman ophiolite and its lithosphere) seismic network.* GEOFON Data Archive. Retrieved from https://www.fdsn.org/networks/detail/5H_2013/ doi: 10.7914/SN/5H_2013

Wu, J., Suppe, J., Lu, R., & Kanda, R. (2016). Philippine Sea and East Asian plate tectonics since 52 Ma constrained by new subducted slab reconstruction methods. *Journal of Geophysical Research: Solid Earth*, *121*(6), 4670–4741. Retrieved 2024-06-28, from https://onlinelibrary.wiley.com/doi/abs/10.1002/2016JB012923 doi: 10.1002/2016JB012923

Yuan, X., Mechie, J., & Schurr, B. (2008). *Tienshan pamir geodynamics project (tipage).* GFZ Data Services. Retrieved from http://geofon.gfz.de/doi/network/7B/2008 doi: 10.14470/2O097102

Yuan, X., Schurr, B., Bloch, W., Xu, Q., & Zhao, J. (2017). *East pamir network.* GFZ Data Services. Retrieved from http://geofon.gfz.de/doi/network/8H/2015 doi: 10.14470/3U7560589977

ZAMG, Zentralanstalt für Meterologie und Geodynamik. (1987). *Austrian seismic network.* International Federation of Digital Seismograph Networks. Retrieved from https://www.fdsn.org/networks/detail/OE/ doi: 10.7914/SN/OE